IEEE Access
Multidisciplinary | Rapid Review | Open Access Journal

Received September 15, 2019, accepted September 25, 2019, date of publication October 1, 2019, date of current version October 17, 2019.

Digital Object Identifier 10.1109/ACCESS.2019.2945030

Dual-Guidance-Based Optimal Resonant Frequency Band Selection and Multiple Ridge Path Identification for Bearing Fault Diagnosis Under Time-Varying Speeds

JUANJUAN SHI, WEIGUO HUANG, CHANGQING SHEN, XINGXING JIANG, AND ZHONGKUI ZHU
School of Rail Transportation, Soochow University, Suzhou 215131, China

Corresponding author: Weiguo Huang (wghuang@suda.edu.cn)

This work was supported in part by the National Natural Science Foundation of China under Grant 51605319, in part by the Natural Science Foundation of Jiangsu Province under Grant BK20160318, and in part by the China Postdoctoral Science Fund under Grant 2017M611896 and Grant 2019T120456.

ABSTRACT To perform bearing fault diagnosis under variable speeds, the optimal resonant frequency (ORF) band selection and diagnosis strategy are pivotal. Indexes, such as kurtosis, crest factor (CF) and smoothness index (SI), are extensively used for guiding ORF selection. Due to that each index has unique advantages, the hybrid of such indexes has been developed. However, applications of the current index hybrid method are impeded by problems of: 1) ineffectiveness for signal corrupted by impulsive noises and 2) equal segmentation of frequency band with human intervention. This paper, therefore, firstly proposes a dual-guidance based scheme with an embedded tunable Q-factor wavelet transform (TQWT) to address the problems. The so-called dual-guidance scheme contains two guidance procedures: 1) the SI guided pre-process for obtaining weight vectors and 2) the index hybrid output guided scheme for ORF selection. The embedded TQWT is used for frequency band segmentation and sub-band signal acquisition without subjective interventions. With the proposed scheme, the ORF band can be determined for bearing fault feature extraction. Then, an algorithm for multiple instantaneous frequency (IF) ridge identification is exploited based on the peak search algorithm for diagnosis. To tackle the difficulty that, at each time instance, the amplitudes of IF ridges of interest do not always dominate the time frequency representation (TFR), a starting point search tactic with a synchronization step is explored. A diagnosis vector can subsequently be obtained by calculating the average ratios of the identified ridges and bearing fault diagnosis can then be done by matching the elements of the diagnosis vector with fault characteristic coefficient (FCC). Comparisons are performed to illustrate the superiority of the proposed method. The experimental analyses are also conducted to validate the proposed method for bearing fault diagnosis under variable speeds.

INDEX TERMS Variable speed condition, bearing fault diagnosis, index hybrid, optimal resonant frequency, time frequency ridge extraction, fault feature extraction.

NOMENCLATURE

FCC	Fault characteristic coefficient
SK	Spectral kurtosis
IF	Instantaneous frequency
SNR	Signal to noise ratio
IFCF	Instantaneous fault characteristic frequency
STFT	Short time Fourier transform
IH	Index hybrid
TFA	Time frequency analysis
ISRF	Instantaneous shaft rotating frequency
TFR	Time frequency representation
ORF	Optimal resonant frequency
TQWT	Tunable Q-factor wavelet transform

The associate editor coordinating the review of this manuscript and approving it for publication was Nagarajan Raghavan.

I. INTRODUCTION

Bearings are one of key components in rotating machinery; thus their fault detection and diagnosis have long been investigated to prevent severe equipment damage and unscheduled downtime [1], [2]. When a fault in one surface of a bearing interacts another surface, an impulse is generated which excites resonances in the system. These impulses are the main features to be detected to perform bearing fault diagnosis, regardless of bearing working conditions (constant speeds or variable speeds). For constant speed conditions, once these impulses are extracted, the frequency of impulse repetition can be obtained by frequency analysis, which is related to the fault existence and fault category [3]–[5]. However, when the rotational speed is unstable, the speed fluctuations may cause ''smearing'' of the discrete frequencies in the frequency representation, indicating that these frequencies are no longer detectable [6]. As a result, approaches developed for bearing fault diagnosis under a constant speed would be ineffective. Order tracking has proven powerful in bearing fault detection under variable speeds [7]. Nevertheless, order tracking unavoidably propagates error to the result because the resampling is achieved via polynomial interpolations, while vibration signals are generated by cyclic phenomena and thus sinusoidal not polynomial in nature [8]. Moreover, order tracking might render the carrier frequencies of the transient responses extend to a wider scope as natural characteristics of bearing system rarely vary, which is not conductive to bearing fault feature extraction [9]. Fortunately, time frequency analysis (TFA) provides an alternative for bearing fault diagnosis under time-varying speeds; it, therefore, has strong potential to characterize the vibration signals of bearings working in nonstationary speed conditions. However, even if a clear TFR can be obtained with extracted fault signatures, bearing fault diagnosis cannot be fulfilled yet as the fault type cannot be determined without knowing the relationship of the IF ridges on the TFR. Thus, it can be concluded that there are two major tasks to perform an effective bearing fault diagnosis under variable speed operations: fault feature extraction and IF ridge identification from TFR.

Numerous techniques and tools have been developed for bearing fault feature extraction. One of the most straightforward methods is to filter signals by identifying the ORF band [10], [11]. Lin and Qu utilized wavelet analysis for the optimal band pass filter design based on the wavelet entropy minimization method [12]. Later, Qiu et al. attempted to combine Shannon entropy with a periodicity detection method to select Morlet wavelet parameters for the wavelet filter for bearing fault detection [13]. Bozchalooi and Liang adopted SI for wavelet parameter determination and then they extended the application of SI for band-pass filter design for bearing fault diagnosis [14], [15]. He et al. suggested to fuse Morlet wavelet filter and sparse code shrinkage to identify bearing fault signatures [16]. Wang et al. introduced a general sequential Monte Carlo method to optimize a complex Morlet wavelet filter for bearing fault feature extraction, which successfully determined the optimal center frequency and bandwidth [17]. In addition to wavelet-based filter, spectral kurtosis (SK) has been also proven an effective tool in locating the ORF band for rotating machinery fault diagnosis [18]. However, the complete exploration of a whole plane $(f, \Delta f)$ is a challenging task (f and Δf representing frequency and frequency resolution, respectively), which confines the industrial application of SK. To address such a problem, a fast algorithm of kurtogram is proposed for computing the kurtogram over a dyadic grid in the $(f, \Delta f)$ plane [19]. Along this line, improved kurtogram-based algorithms have been exploited to enhance the capability of locating OFR band for rotating machinery condition monitoring [20]–[23]. All the aforementioned SK-related methods are based on a fact that the kurtosis can effectively measure the impulsiveness of signals. However, kurtosis does not always truly reflect the signal impulsiveness when the signal to noise ratio (SNR) is low and non-Gaussian noise exists, as stated by Moshrefzadeh and Fasana [24]. They then modify forms of kurtosis and propose the Autogram for selecting the optimal demodulation band. Before Autogram, Antoni also advances the SK method by proposing to measure the negentropy of the squared envelope and squared envelope spectrum of signals, from which the squared envelope infogram and squared envelope spectrum infogram are generated for identifying ORF of signal with impulsive noise [25]. The infogram is an extension of kurtogram, extending the domain of applicability of the kurtogram. However, as reported in ref. [26], negentropy cannot quantify the repetitive transients masked in strong random noise.

Different from the approaches mentioned above, Bozchalooi and Liang suggest to develop indexes which can tackle signals with impulsive noise. They propose an index, i.e., SI, to measure the signal impulsiveness [14]. Besides, crest factor (CF) is also employed as an index to guide the Morlet wavelet demodulation [27]. Further, due to that each index has the exclusive virtues, an algorithm which fuses the three indexes (i.e., kurtosis, CF and SI) to guide the ORF band selection is proposed by Li *et al.* [28], where the processing results of simulated and experimental data validates the superiority of the proposed method, compared with using a single index. However, there are two issues requiring to be taken into consideration to further improve the detectability of the fusion method: (1) multiple indexes may fail to cooperatively work towards the ORF band selection because one or two of the indexes may have large values caused by outliers or interfering signals and still play a leading role to determine the ORF band due to fixed weights; whereas functions of other indexes may be weakened; and (2) the frequency band are empirically segmented equally.

Moreover, it has to mention that most of the aforementioned techniques are applied for bearing fault diagnosis under in-variant speed conditions. In the content of time-varying speeds, bearing health condition monitoring cannot be done yet only with the selected ORF band. As stated above, a resampling-free method is preferred [9], [29] and thus TFA becomes an alternative due to its advantages in

non-stationary signal analysis. The diagnosis can be performed by identifying the IF ridges on the obtained TFRs and then calculating their ratios. Related research has been conducted in this direction. Shi et al. develop a novel TFA method to gain a clear TFR and then apply it for bearing fault diagnosis by computing the point-to-point ratios between IF ridges [30]. Huang et al. propose to use a fast path optimization algorithm for multiple IF ridge extraction from the TFR [31]. Then, the average curve-to-curve ratios are utilized to achieve the fault diagnosis. The key step of such TFR-based algorithms for bearing condition monitoring is to accurately extracted the IF ridges of multiple signal components. The mentioned two techniques are effective in time frequency curve extraction; however, they are sensitive to strong noise as no de-nosing operation is involved. Most fundamental IF ridge extraction methods are performed via searching the frequency bins with maximum energy at each time instance [32], which is extensively used for IF estimation of non-stationary signals as it is easy to be implemented with computational efficiency. Nevertheless, this kind of methods are based on the assumption that at each time instance the IFs of interest have the maximum amplitude on TFR, which is not always true, particularly for the multi-component signal with low SNR under variable speeds. To solve this issue, Wang et al. developed a novel amplitude-sum based spectral peak search algorithm, where, for each frequency bin, the sum of the amplitudes of its several multiples is calculated to replace the original amplitude [33]. The effectiveness of this algorithm is likely to be weakened if the signal contains shaft-synchronized signal components caused by other machine components, such as gears. Moreover, to perform bearing fault diagnosis under variable speeds without using resampling which is error-prone in the noisy environment, a single extracted IF ridge is not sufficient [30], [31].

In view of the above, this paper first proposes a dual-guidance based scheme with TQWT embedded for ORF band selection to maximally extract the defect-induced impulses. The proposed scheme is devised to address the issue that the three indexes may fail to jointly contribute to the ORF selection for signal with impulsive noise. The utilization of TQWT aims to tackle the second aforementioned problem that the frequency band is subjectively divided equally. The frequency responses of TQWT can partition the frequency band following the pattern that the frequency resolution increases with the decrease of frequency, which satisfies the requirement that high frequency can accept a lower frequency resolution whereas low frequency requires a higher frequency resolution. A peak amplitude search based multiple IF ridge identification method with a synchronization step and novel starting point search tactics involved is subsequently developed for bearing fault diagnosis. With the extracted IF ridges, the bearing fault diagnosis can be conducted using a diagnosis vector with elements consisting of the average ratios among the extracted IF ridges.

The rest of the paper is organized as follows. Motivations of the proposed method are given in Section 2.

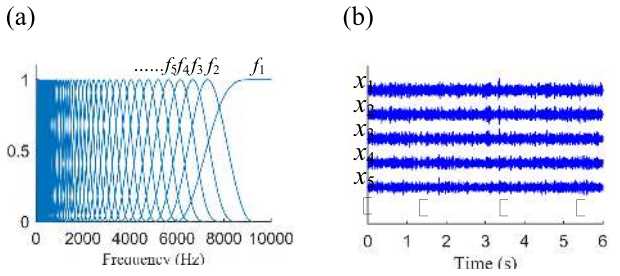

FIGURE 1. Frequency response of TQWT with $Q = 4$, $r = 5$, $J = 60$: (a) the frequency response, and (b) the corresponding sub-band signals.

Section 3 presents the proposed dual-guidance based ORF band selection scheme, the algorithm for multiple IF ridge path identification and the diagnosis strategy. Experiment validations of the proposed method are shown in Section 4. The conclusions are summarized in Section 5.

II. MOTIVATIONS OF THE PROPOSED SCHEME

Prior to the presentation of the proposed method, the motivations are firstly demonstrated in the following.

A. SUMMARY OF TQWT AND ORIGINAL INDEX HYBRID METHOD

To begin with, TQWT proposed in ref. [34] is employed to segment the entire frequency band into a string of sub-frequency bands and each of the sub-frequency bands corresponds to a band-pass filter. If the sub-frequency band combinations corresponding to the ORF of the vibration signal could be detected, the fault-induced impulses can then be maximally extracted, paving the way for further TFA and bearing fault diagnosis. TQWT is determined by three parameters, including Q-factor Q, redundancy r and decomposition stage J. Once parameters r, Q and J are specified, a TQWT-generated frequency response is determined. More details regarding TQWT can be found in ref. [34]. With a specific TQWT-related parameter set, the frequency response can then be obtained, as shown in FIGURE 1 (a). Each sub-frequency band corresponds to each sub-signal given in FIGURE 1 (b). For ORF selection, the main objective is to adaptively select one or several sub-frequency bands to maximally extract bearing fault induced impulses.

Based on TQWT for frequency band partition, Luo et al. proposed a kurtosis-guided method for adaptive demodulation for bearing fault diagnosis and the effectiveness of this method has been validated by experiments [35]. For an N-point signal x, kurtosis is defined as

$$kurtosis(x) = \frac{\sum_{i=1}^{N} (x_i - \bar{x})^4 / N}{\left(\sum_{i=1}^{N} (x_i - \bar{x})^2 / N\right)^2}, \tag{1}$$

where $\bar{x}$ denotes the mean of the signal sequence. However, as illustrated in ref. [14], the effectiveness of kurtosis as an impulsiveness measure in the context of bearing condition monitoring would be undermined by the over-sensitivity to

outliers, the dependency of kurtosis on rotational speed and the lack of a meaningful benchmark to be used to distinguish the level of impulsivity. To address such problems, Bozchalooi and Liang proposed to replace the kurtosis by SI to measure the impulsiveness of signals [14]. For a signal $x(n)$ with the length of N, the SI is defined as the ratio of the geometric mean and the arithmetic mean to the signal series, i.e.,

$$SI(x) = \frac{\left(\prod_{n=1}^{N} x(n)\right)^{1/N}}{(1/N)\sum_{n=1}^{N} x(n)}. \tag{2}$$

A property of SI is that it approaches unity for flat time series and drops to zero for a highly impulsive series. Furthermore, SI is not easily influenced by outliers, as indicated in [14]. The drawback of SI, however, is that it is incapable of distinguishing signals with low SI values [28]. Thus, Li et al. developed an index hybrid technique for spectral segmentation, where the kurtosis, SI and crest factor (CF) are jointly applied. CF is a measure of a waveform, such as sound or vibration signals, showing the ratio of peak values to the effective value. In other words, CF indicates how extreme the peaks are in a waveform. CF equaling 1 manifests no peaks and higher CF values indicate impulsiveness. It is defined as the ratio of the peak amplitude to the root mean square (RMS) of the signal

$$CF(x(n)) = \frac{\max(x(n)) - \left(\sum_{n=1}^{N} x(n)\right)/N}{\sqrt{\left(\sum_{n=1}^{N} x^2(n)\right)/N}}. \tag{3}$$

The joint application makes the three measurements mutually complement and yields a better outcome for spectral segmentation [28]. Motivated by this, it can be foreseen that the index hybrid strategy has a great potential application to ORF determination for bearing condition monitoring. The single function which fuses multiple indexes is defined as [28]

$$IH\left(x_i(t)\right) = F\left(I_q(x_i(t))\right), \tag{4}$$

where $IH\left(x_i(t)\right)$ represents the index hybrid output of signal $x_i(t)$, $x_i(t)$ denotes the ith sub-band signal obtained by inverse TQWT, as shown in FIGURE 1, $F(\cdot)$ stands for the hybrid of indexes, and I_q denotes the qth index ($q = 1$, 2, and 3, representing the index of kurtosis, CF and the reciprocal of SI, respectively). In such a way, it can be concluded that a high level of impulsivity leads to a large output of Eq. (4). The three indexes work together to determine the output of the function. The difference is that each one weighs variously for different signals. Ideally, the index which can provide more useful information should be given a greater weight. To determine the weight of each index, the information entropy, a measure of the disorder degree of data, is utilized. High inhomogeneity of the distribution of an index indicates low entropy of the index, namely an index with a lower entropy should be given more weights [28]. With the weight for each index being determined, multiple indexes can be hybrid. The original index hybrid steps are summarized in the following.

1. Normalize each index I_q using the equation below (5), as shown at the bottom of the next page where $I'_q\left(x_i(t)\right)$ represents the normalized value of each index for the ith sub-band signal, $x_i(t)$ denoted the ith sub-band signal generated by inverse TQWT.

2. Calculate the entropy E_{q} of each index using

$$E_q = \frac{1}{\ln(J+1)} \sum_{i=1}^{J+1} P_q\left(x_i(t)\right) \ln\left(P_q\left(x_i(t)\right)\right), \tag{6}$$

where $P_q\left(x_i(t)\right) \ln\left(P_q\left(x_i(t)\right)\right) = 0$ when $P_q\left(x_i(t)\right) = 0$, P_q is the probability of the $I'_q\left(x_i(t)\right)$ presenting in the sequence $\left[I'_q\left(x_1(t)\right), I'_q\left(x_2(t)\right), \ldots, I'_q\left(x_{J+1}(t)\right)\right]$ and calculated by $P_q\left(x_i(t)\right) = I'_q\left(x_i(t)\right) \Big/ \sum_{i=1}^{J+1} I'_q\left(x_i(t)\right)$.

3. Determine the weight W_q for the qth normalized index by

$$W_q = \frac{1 - E_q}{\sum_{q=1}^{3}(1 - E_q)}. \tag{7}$$

Then Eq. (4) can be re-formed as

$$IH\left(x_i(t)\right) = \sum_{q=1}^{3} \left(W_q I'_q(x_i(t))\right). \tag{8}$$

The hybrid strategy detailed above takes advantages of complementary signatures of the indexes and has the potential of being used to guide the ORF band selection.

B. MOTIVATION ILLUSTRATION

With the TQWT for frequency band segmentation, the procedure of the ORF selection is that: a) the sub-band signals corresponding to (J+1) stages of TQWT are firstly generated; b) the merging operation of neighboring sub-band signals is implemented if the current merging forms a signal with a higher IH output calculated by Eq. (4); otherwise the sub-signal is remained unchanged and the process turns to the next sub-band signal; c) step b) is repeated under the guidance of the IH output until all the sub-band signals have been involved.

However, when vibration signals collected from rotating machinery under variable speed conditions are polluted by extensive background noise and outliers which may be generated by unexpected strikes during the operation, the ORF would be improperly selected using the original index hybrid method detailed above. The reason is that both kurtosis and CF values are over-vigilant to such outliers. Thus, kurtosis and CF would play a leading role when selecting the frequency band since the weight for each of them is fixed; whereas the contribution of SI which is negligibly affected by outliers would be weakened, thus leading to an inappropriate ORF selection.

To illustrate, a simulated signal containing fault-induced impulses under time-varying speed operation, cyclic interferences and outliers are constructed. The simulated signal $x(t)$ is a mixture of bearing fault induced impulses $x_1(t)$, white Gaussian noise $n(t)$, interferences $x_{int}(t)$ and random

TABLE 1. Parameters of the simulation model.

Parameters	N	f_s	ω_r	β	η	A	FCC	N_I
value	120000	20 kHz	2 kHz×2π	800 Hz	0.7	4/3	3.7	3

interfering impacts $x_{imp}(t)$

$$x(t) = x_1(t) + n(t) + x_{int}(t) + x_{imp}(t). \tag{9}$$

The impulsive signal of faulty bearing under ramp-down speed is firstly generated. The model of vibration signal collected from faulty bearing under unstable speed operation can be written as [36]

$$x_1(t) = \sum_{l=1}^{L} A_l e^{-\beta(t-t_l)} \sin(\omega_r(t-t_l))\mathrm{u}(t-t_l), \tag{10}$$

where L is the signal length, $A_l = A(N/f_s - \eta t_l)$ is amplitude which is inversely proportional to time instant t_l since the bearing works under a speed-down case, A and η are constants, $n(t)$ is the white Gaussian noise, and t_l is the occurrence time of the lth impulse ($l = 1, 2, \ldots$). The parameters associated with the simulation model is listed in TABLE 1. More details about the impulsive-like signal generation under time-varying speed can be found in ref. [36]. The instantaneous shaft rotating frequency (ISRF) and simulated FCC is set to $f_r(t) = -1.25t + 35$ and 3.7, respectively, in this study. SNR is set to -12 dB. In addition to background noise $n(t)$, vibration signals of faulty bearing are often polluted by cyclic interferences $x_{int}(t)$ which is constituted by two parts. The first part $x_{int\_1}(t)$ is often resulted by mechanical or/and electrical components, thereby a cyclic interferences with a constant frequency 60 Hz and amplitude 1 being added into the simulated signal. Meanwhile, to reflect the phenomena of misalignment, imbalance or/and eccentricity, the other part $x_{int\_2}(t)$ is composed of the cyclic interferences with the shaft rotational frequency and its harmonics as the frequencies, i.e., $x_{int\_2}(t) = \sum_{i=1}^{I} A_i \cos(2\pi k_i f_r(t)t)$. Three shaft speed related signal components are taken into consideration, therefore k_i ($i = 1, 2, 3$) equals 1, 2, 3. The amplitude A_i ($i = 1, 2, 3$) is set to 1.25, 1.5,1 for each signal component. Apart from the impulses induced by bearing localized fault, vibration signals might be contaminated by other random impacts [14]. Hence, two outliers, i.e., x_{imp}, are mixed into the simulated signal. The simulated signal mixture and the TFR of its envelope is shown in FIGURE 2 (a) and (b), respectively.

To extract the impulses from the simulated signal, one of the effective methods is to identify the ORF band and then band-pass filter the signal. The original index hybrid strategy stated above is used for this purpose. Processing results are shown in FIGURE 3. The Q-factor Q and redundancy r are

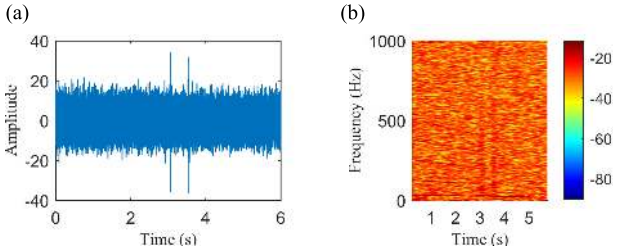

FIGURE 2. The simulated signal and its TFR: (a) simulated signal in time domain, and (b) STFT-generating TFR of the envelope of the simulated signal.

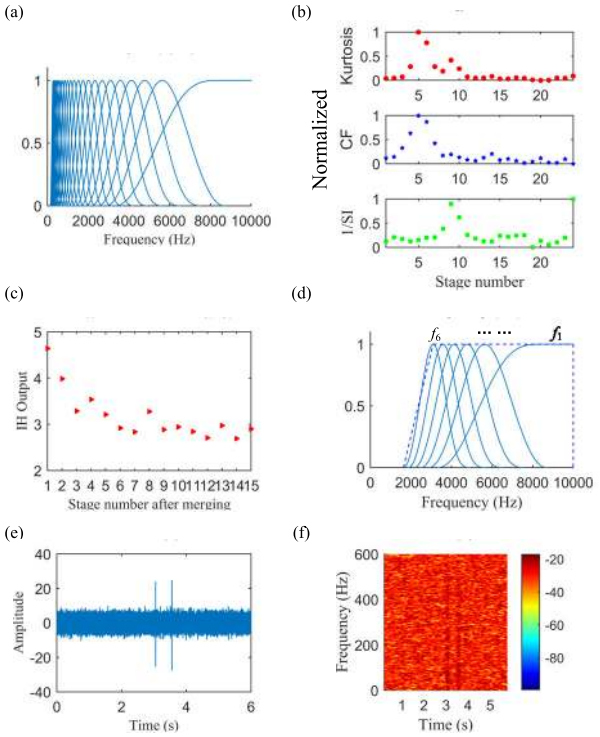

FIGURE 3. Processing results of the simulated signal using original index hybrid strategy: (a) frequency responses of TQWT; (b) original kurtosis, CF and reciprocal of SI of each sub-signal; (c) IH output of each merged signal; (d) selected ORF band; (e) filtered signal using the selected ORF band; and (f) TFR of the filtered signal envelope. (Note: Unit of the simulated signal can be arbitrary)

determined as 2 and 5, respectively (details are presented in subsection 0). The number of stages is calculated by Eq. (19). The resulted frequency response is presented in FIGURE 3 (a). FIGURE 3 (b) shows the kurtosis, CF and the reciprocal of SI values of each subsignal. The index hybrid output (IH output) is achieved by fusing the three indexes following the manner detailed above. The larger IH output means the higher level of impulsivity.

The resulting IH output is shown in FIGURE 3 (c) and the selected sub-frequency bands are exhibited in FIGURE 3 (d).

$$I_q'(x_i(t)) = \frac{I_q(x_i(t)) - \min\left[I_q(x_1(t)), I_q(x_2(t)), \ldots, I_q(x_{J+1}(t))\right]}{\max\left[I_q(x_1(t)), I_q(x_2(t)), \ldots, I_q(x_{J+1}(t))\right] - \min\left[I_q(x_1(t)), I_q(x_2(t)), \ldots, I_q(x_{J+1}(t))\right]}, \tag{5}$$

It can be seen that the center frequency of the selected band-pass is around 6000 Hz, largely deviating from the pre-set resonant frequency 2000 Hz. The signal is then purified using the selected filter centered at 6000 Hz, resulting the filtered signal in FIGURE 3 (e). STFT-resulting TFR of the envelope of the filtered signal is presented in FIGURE 3 (f), where no IF-ridges related to instantaneous fault characteristic frequency (IFCF) and its harmonics can be easily recognized as the ORF is improperly selected. This example demonstrates that the ORF for bearing fault diagnosis might be mistakenly selected if the vibration signal contains outliers when using the original criterion fusion strategy. The underlying reason is that two of the three indexes are over-sensitive to impulsive noises while the weight for three indexes are almost identical due to that the indexes present the similar changing pattern, resulting the incorrect frequency band is selected (weights equals 0.3214, 0.3466 and 0.3320, respectively, according to Eq. (7)).

III. PRESENTATION OF THE PROPOSED METHODOLOGY

To correctly determine the ORF of signals corrupted with impulsive noise and harmonic interferences, the proposed method for bearing fault diagnosis under unstable rotational speed conditions is detailed in this section, which is constituted by three parts, including the dual-guidance based ORF selection, multiple ridge path identification and diagnosis strategy. Each part is elaborated in the following section.

A. DUAL-GUIDANCE BASED ORF SELECTION SCHEME WITH TQWT EMBEDDED

1) PROPOSED DUAL-GUIDANCE BASED SCHEME FOR ORF SELECTION

To tackle the aforementioned issues, the novel dual-guidance based ORF scheme is proposed. It is known that two of the three indexes, i.e., kurtosis and CF, are sensitive to outliers and shaft rotating speeds; whereas SI is not alert to outliers and operation speeds [14]. Inspired by this observation, we propose to use SI to guide weight vector generation of the other two indexes before hybrid operations, which is the first guidance. The purpose of calculating weight vectors is to make sure that the index correctly reflect the signal impulsiveness is given more weights while the one that does not truly reflect signal impulsiveness is given no weights. Specifically, if the kurtosis and CF change in the same manner as SI (i.e., peaks of three indexes are located in the same intervals), the IH output is calculated using Eq. (4) with constant weights; otherwise, weight vectors of kurtosis and CF vectors are calculated.

Further, TQWT is used to partition the frequency band with desirable frequency resolution, instead of subjective partition. The index hybrid is then performed to guide ORF band selection based on TQWT, which is the second guidance operation. According to the discussion above, the steps of the proposed dual-guidance scheme are elaborated as follows.

1. *Acquire index vectors*. Generate the frequency response and all sub-band signals with determined TQWT-related parameters (details in section 0). Each sub-band signal, i.e., $x_1(t), x_2(t), \ldots, x_i(t), \ldots, x_{J+1}(t)$, corresponds to each sub-frequency filter, as illustrated in FIGURE 1,

$$x_i(t) = \mathrm{TQWT}^{-1}(\boldsymbol{w}_i), \quad i = 1, 2, \ldots, J+1, \tag{11}$$

where $\boldsymbol{w}_i$ represents the wavelet coefficients of the ith stage, and TQWT^{-1} denotes the inverse TQWT. Generate three index vectors of $J+1$ sub-band signals, i.e., $\mathbf{I}_q$, $q = 1, 2, 3$, denoting the kurtosis, CF and reciprocal of SI, respectively.

2. *Calculate weight vectors(first guidance)*. Use SI to guide the weight vector calculation. Denote weight vectors by $\mathbf{W}_q$ ($q = 1, 2, 3$). Comparing peak intervals of vector $\boldsymbol{I}_1$ and $\boldsymbol{I}_2$ with that of $\boldsymbol{I}_3$, If peak intervals of the three vectors are situated in the same region (this can be done by comparing the peak locations of vectors: if their peaks are located at the same stage, then their peak intervals are in the same region; otherwise, their peak intervals are situated at different regions), go to step 3; otherwise, weight vector for Kurtosis and CF vectors are calculated by the following way. Peak interval is defined as the region centered at the maximal value of $\boldsymbol{I}_q$ ($q = 1, 2, 3$) with the boundaries determined by n and n'. The n and n' are stage number located at left and right sides of the current maximal value of $\boldsymbol{I}_q$, respectively, and correspond to the stage number where the index value $I_q(n)$ ($I_q(n')$) is greater than the mean of $\mathbf{I}_q$ and its left (right) neighbor is not greater than the mean of $\mathbf{I}_q$, as shown in FIGURE 6 (a). Elements of weight vector $\mathbf{W}_3$ are equal since SI is not sensitive to outliers and calculated by Eq. (7). Weight vectors $\mathbf{W}_q$ ($q = 1, 2$) are calculate using

$$\boldsymbol{W}_q(i) = \begin{cases} 0, & i \in [n, n'] \\ \dfrac{1 - E_q}{\sum_{q=1}^{3}(1 - E_q)}, & otherwise \end{cases} \quad (i = 1, 2, \ldots, J+1), \tag{12}$$

and Eq. (8) can be re-formulated as

$$IH\ (x_i(t)) = \sum\nolimits_{q=1}^{3} \left(W_q(i) I'_q(x_i(t)) \right), \tag{13}$$

where $W_q(i)$ represents the ith element of vector $\mathbf{W}_q$.

3. *Implement merging operations* (*second guidance*). Utilize the obtained weight vectors to calculate IH output via Eq. (13) to guide the merging operation. Intermediate signal $yim(t)$, which is defined as the signal being processed at the current merging operation, is generated. If the addition of the current sub-band signal $x_i(t)$ to the intermediate signal $yim(t)$ can boost the IH output, the $x_i(t)$ is added to $yim(t)$ to form a new intermediate signal, i.e., $yim(t) \leftarrow yim(t) + x_i(t)$; otherwise, the current intermediate signal remains unchanged and is output, and the new intermediate signal is updated as $yim(t) \leftarrow x_i(t)$. Namely, if $IH\ (yim(t)) < IH\ (yim(t) + x_i(t))$, continue merging the intermediate signal $yim(t)$ with the ith sub-band signal to form the new intermediate signal $yim(t)$; otherwise, keep the intermediate signal $yim(t)$ as an output of merging denoted by $mx_j(t)$ and set the ith sub-band signal $x_i(t)$ as the new intermediate signal $yim(t)$, then switch to merging the next sub-band signal with the new $yim(t)$. Repeat

The pseudo-code for merging operation

Initialization:

Set number of sub-signals J and initialize intermediate signal $yim(t)=x_1(t)$, $j=1$.

While $i \le J+1$

Calculate IH output of $yim(t)$ and $yim(t)+x_i(t)$;

If $IH\left(yim(t)\right) < IH\left(yim(t)+x_i(t)\right)$, **then**

Update $yim(t) \leftarrow yim(t)+x_i(t)$;

Else then

Output the current $yim(t)$ as merged signal $mx_j(t)$ and update $yim(t) \leftarrow x_i(t)$;

Update $i \leftarrow i+1, j \leftarrow j+1$;

End

Ouput J^* merged signals, i.e. $mx_1, mx_2, ..., mx_j, ..., mx_{J^*}$

FIGURE 4. Pseudo code of merging operation.

the process until all sub-band signals are involved, resulting J^* output signals. The pseudo code of the merging operation is shown in FIGURE 4.

4. *Select ORF band*. Find out the merged signal with maximal IH output denoted by $mx_{j^{opt}}$, which can be formulated as

$$\begin{aligned} mx_{j^{opt}}(t) &= x_k(t) + x_{k+1}(t) + \ldots + x_{k+m}(t), \\ &\quad k \in (1, 2, \ldots, J), \quad m \in (0, 1, \ldots, J-k), \\ subjected\ to: \ j^{opt} &= \arg\max_j \left(IH\left(mx_j(t)\right)\right), \\ &\quad j = 1, 2, \ldots, J^*, \end{aligned} \tag{14}$$

which means that the selected merged signal is composed by $m+1$ sub-band signals starting from the kth sub-band signal. Output the corresponding merged sub-frequency band $f_{m(j^{opt})}$ determined by $[f_k f_{k+m}]$, which is the selected ORF band using the proposed scheme.

The developed dual-guidance based ORF band selection is graphically presented in the flowchart of FIGURE 5. The determined ORF band corresponds to the merged signal segment with the maximum IH output calculated by Eq. (13).

To validate the effectiveness of the proposed dual-guidance based scheme for ORF determination, the simulated signal defined by Eq.(9) in Section 0 is processed. FIGURE 6 shows the processing results. The normalized indexes are shown in FIGURE 6 (a), where peak intervals of kurtosis and CF are located at different regions with that of SI. The black dashed lines in FIGURE 6 (a) represents the mean of kurtosis and CF vectors, respectively. For kurtosis vector, n and n' equal to 4 and 6, respectively, as presented in FIGURE 6 (a); thus, the peak interval is [4], [6]. Likewise, the peak interval for CF can also be obtained [3], [7] from FIGURE 6 (a). The weight vectors are then calculated, as shown in FIGURE 6 (b). With the weight vectors, IH output can be obtained. The IH output of signals which are merged by the guide of the index hybrid scheme is presented in FIGURE 6 (c), where the maximal

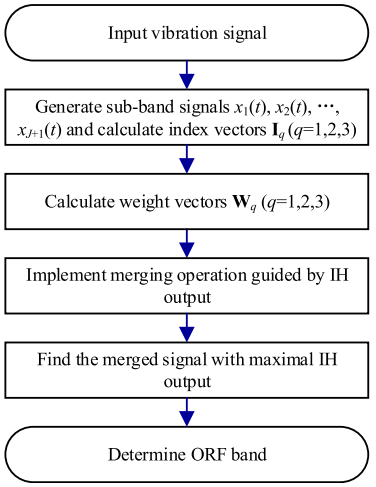

FIGURE 5. Flowchart of the proposed dual-guidance based ORF selection scheme.

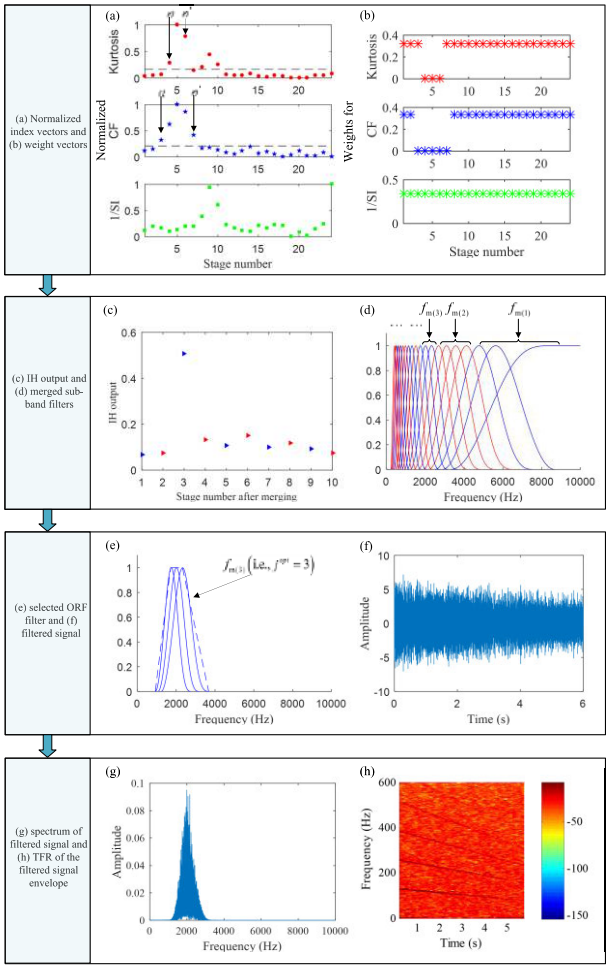

FIGURE 6. Processing results of the simulated signal in Section 2 using the proposed dual-guidance based scheme ($f_m(j)$ represents the j th merged filter).

IH output can be easily identified. The 3rd merged signal $mx_3(t)$ yields the maximal IH output (i.e., $j^{opt} = 3$), which is constituted by three sub-band filter. From FIGURE 6 (d), it can be seen that the 8th, 9th and 10th sub-band filters of the

original frequency response (before merging) composes the 3rd merged signal; hence parameters m and k can be identified as $k = 8$, $m = 2$. The selected ORF is plotted in FIGURE 6 (e). The raw signal is then filtered using the selected ORF band, resulting the filtered signal in FIGURE 6 (f). FIGURE 6 (g) shows the spectrum of the filtered signal using the selected ORF band, where it can be seen that the signal frequency is almost centered at 2000 Hz, identical to the pre-set resonant frequency. The vibration signal is then demodulated and time-frequency analyzed using Hilbert Transform and STFT, respectively. The resulting TFR is exhibited in FIGURE 6 (h). As seen, the IFCF and three its harmonics can be recognized, indicating that the adverse effect of harmonic interferences and unexpected outliers on ORF determination are eliminated using the proposed dual-guidance based ORF selection scheme.

Compared with the results (shown in FIGURE 3) obtained by the original index hybrid strategy, the ORF band can be properly selected using the proposed scheme as fixed weights are replaced by weight vectors to make sure that the vigilance of kurtosis and CF to outliers and speed variations are weakened and the three criteria then jointly work towards the ORF determination.

2) PARAMETER DETERMINATION OF TQWT FOR ORF SELECTION

The proposed dual-guidance based ORF selection is based on frequency responses generated by TQWT. As stated previously, TQWT is a kind of wavelet transform with tunable parameters, including Q-factor (Q), redundancy (r), and the number of stages (J). The determination of such parameters inevitably has influences on the effective realization of TQWT for ORF selection. There are numerous types of combination of Q, r and J. In order to guide the parameter selection of TQWT for ORF band determination, the effects of these parameters on frequency response are analyzed.

Our focus of using TQWT is on the ORF selection to extract the fault-generated impulses as much as possible; hence, the bandwidth of each sub-frequency band, which corresponds to a band-pass filter, is vital for the success of the proposed scheme. A wide sub-frequency band would result in a low frequency resolution; while a narrow one would lead to a high frequency resolution, which is desirable by the proposed scheme. According to ref. [34], the bandwidth of the frequency response producing sub-frequency band j is approximately half the width of the interval over which the frequency response is non-zero. Using this approximation, the bandwidth of jth sub-frequency band can be calculated by

$$BW_j = \frac{1}{2}\beta\alpha^{j-1}\pi. \tag{15}$$

The scaling parameters α and β can be expressed by

$$\alpha = 1 - \frac{\beta}{r}, \quad \beta = \frac{2}{Q+1}. \tag{16}$$

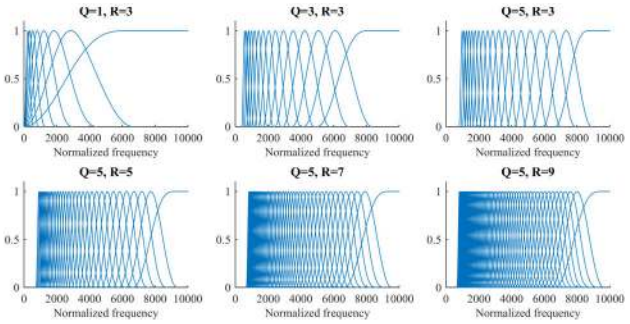

FIGURE 7. Frequency responses of TQWT with different parameter combinations (data length N is 250, number of stages J adopts the maximum. The calculation of maximal J can refer to ref. [28]. Note that the low frequency is not covered in these figures as the signal length is only 250.).

From Eqs.(15) and (16), it can be deduced that an increase of Q will narrow the bandwidth of each sub-frequency response if the redundancy r is fixed. This observation can also be echoed by observing the first row of FIGURE 7. However, Q cannot be unlimitedly large as its increase could incur the decrease of the covering frequency range. The covering frequency range is defined as the frequency range that the frequency response of TQWT can reach. Without losing the generality, the lowest frequencies f_{low} that frequency responses can reach versus different Q-factors is plotted in FIGURE 8, where it can be seen that the lowest frequencies covered by frequency responses drop with the increase of Q. In addition, the computation cost is also boosted by the increase of Q for the index hybrid guided ORF determination algorithm. This is because the number of stage J grows with the augment of Q and consequently more sub-frequency bands are involved for computation. The computational complexity of the whole algorithm can be approximated as $O(J)$, indicating that execution time of the algorithm is linear in J. Therefore, Q represents a compromise among the band-pass bandwidth, frequency range and computational cost. The effect of redundancy r on bandwidth of sub-frequency bands is similar to that of Q, i.e., the bandwidth becomes narrow with the increase of r when Q being fixed according to Eq.(15) and Eq.(16). In terms of the covering frequency range and computational cost, the former slightly declines when r increasing, as shown in FIGURE 8, and the latter boosts with the increase of r because the number of stage J of TQWT increases according to the following equation [34]

$$J_{max} = \left\lfloor \log(N/4(Q+1))/\log\left(1/(1-2/(r(Q+1))\right)\right\rfloor \tag{17}$$

where $\lfloor z \rfloor$ stands for the largest integer that is less than z.Therefore, the growth of r would substantially augment the computational cost since it linearly increases with J. As can be observed in FIGURE 8, the covering frequency range is negligibly affected by the increase of the redundancy r. Thus, r can be determined by achieving a desirable trade-off between the bandwidth and computational cost. The number of stages has few effects on the bandwidth of each

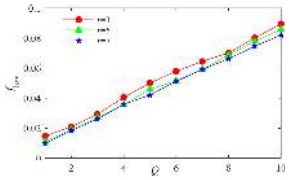

FIGURE 8. Frequency range that the frequency response can cover under different parameter combinations (data length N is 250, number of stages J adopts the maximum, f_{low} represents the lowest normalized frequency that the frequency response of TQWT can reach).

TABLE 2. Effects of TQWT-related parameters for optimal resonant frequency selection.

Parameters	Bandwidth	Covering frequency range	Computational cost
Q	↓ if Q ↑	↓ if Q ↑	↑ if Q ↑
r	↓ if r ↑	↑ if r ↑	↑ if r ↑
J	No obvious effects	↑ if J ↑	↑ if J ↑

sub-frequency band and can be determined by taking the covering frequency range and computational cost into consideration. The effects of each parameter on bandwidth of each band-pass filter, covering frequency range and computational cost are summarized in TABLE 2.

With the analysis above, the general principle for determining the TQWT-related parameters is to 1) keep the bandwidth of sub-frequency band narrow enough, 2) cover enough frequency range to ensure that the possible resonant frequency bands are not left out and 3) minimize the computational cost. To do so, the Q-factor Q and redundancy r cannot be too large as it will greatly boost the number of stages J and computational cost. Therefore, the range of the redundancy factor r is fixed for a desirable trade-off between the bandwidth and computational cost. The maximum Q adopts 10 by compromising among the bandwidth, covering frequency range and computational cost. The number of stages J for ORF selection is not necessary to take the maximum value since the resonant frequency of bearing systems is often thousands of Hertz. The center frequency of each band-pass filter can be calculated using the following equation [34]

$$f_{c_j} = \alpha^j \frac{2-\beta}{4\alpha} f_s, \quad j = 1, 2, \ldots, J_{\max}, \tag{18}$$

where f_{c_j} represents the center frequency of the jth sub-frequency band and f_s is the sampling frequency. To ensure that the resonant frequency of bearing systems is not left out, the lowest frequency that the frequency response can reach should be not less than f_{bd}, where f_{bd} is a threshold that resonant frequency of most bearing systems can be encompassed. To achieve this, for a determined combination of Q and r, the number of stages J can then be calculated by

$$J = \log_{\alpha} \frac{4\alpha f_{bd}}{f_s(2-\beta)}, \tag{19}$$

where f_{bd} is a user-specified parameter. J can then be determined using Eq. (19) when the lower cut-off frequency f_{bd} is specified by considering covering all possible resonant frequencies of analyzed bearing systems. With the fixed range for Q and r, the combination which is optimal for the signal analyzed is determined using the strategy introduced below.

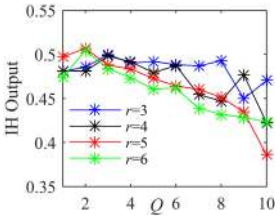

FIGURE 9. IH output- Q scatter diagram.

As described above, the index hybrid strategy yields a better outcome for ORF selection, which also suggests that the IH output can also be employed to determine the optimal Q and r combination for the signal analyzed. The optimal combination can be found using

$$Q, r = \arg\max_{Q,r} \; IH\left(y(t)\right), \quad s.t.\; Q \in [1, Q_{\max}], \quad r \in [r_{\min}, r_{\max}], \tag{20}$$

where $y(t)$ represents the filtered signal using the proposed index hybrid guided scheme. Given the range of parameters Q and r, the optimal Q and r combination corresponds to the merged signal with the maximum IH output. Parameters Q and r for the simulated signal in Section 0 can then be determined as 2 and 5, respectively, as shown in FIGURE 9.

B. MULTIPLE RIDGE PATH IDENTIFICATION

ORF can be determined using the proposed dual-guidance based scheme with the embedded TQWT. Impulse-like signals can then be extracted. However, bearing health condition monitoring is not completed yet since the fault types are not diagnosed only with the filtered signal. Hence, a diagnosis method based on multiple ridge path identification is developed in the following. To conduct the diagnosis, extraction of IFCF and ISRF is critical. In reality, even though the proposed dual-guidance based ORF scheme can facilitate the identification of ridge paths, it cannot make sure that IFCF, ISRF and their harmonics are accurately extracted as the associated signal components might be still faint for weak faults. Dynamic programming algorithms, like the Viterbi algorithm, have been explored to extract ridge paths [37], [38]. Nevertheless, the application of such algorithms might be confined by the taxing computation cost. This paper, therefore, proposes a fast as well as effective method for multiple ridge path identification based on the peak search algorithm which is a fundamental IF extraction method [30], [32].

To begin with, the TFR of the signal analyzed has to be obtained. Since STFT is a powerful tool for TFA of nonstationary signal, the TFRs in this paper are obtained via STFT. For a signal $x(t)$, its STFT can be defined as

$$X(t,f) = \int_{-\infty}^{+\infty} x(\tau) w(\tau - t) e^{-j2\pi f \tau} d\tau, \tag{21}$$

The pseudo-code for 'Algorithm I'

Initialization:

Find starting point (t_m, f_m) where maximum energy in TFR is located and the number of time instants M, set sub-region from $(t_m, f_m\text{-}\Delta f)$ to $(t_m, f_m\text{+}\Delta f)$ zero;

Set parameters, i.e., the pre-determined parameter Δf;

Assign r=m+1, l=m-1, f_r=f_m, and f_l=f_m.

Repeat:

Find $f_{ind} = \arg\max_{f\in(f_{ind}-\Delta f, f_{ind}+\Delta f)} P(t_{ind}, f)$ and let $IF(t_{ind}) = f_{ind}, ind = r, l$;

Set zeros for sub-regions from $(t_{ind}, f_{ind} - \Delta f)$ to $(t_{ind}, f_{ind}+\Delta f), ind = r, l$;

Update $r \leftarrow r$+1 and $l \leftarrow l$-1;

Until l=0 and r=M;

Output the IF (i.e., $IF(t)$).

FIGURE 10. Pseudo code of 'Algorithm I'.

where $w(t)$ should be a low-pass filter, $X(t, f)$ can be interpreted as the correlation between $x(\tau)$ and $w(\tau - t)e^{-j2\pi f\tau}$, and $w(\tau - t)e^{-j2\pi f\tau}$ is compactly time and frequency supported, with energy concentrated at time t and frequency f. Therefore, $|X(t, f)|^2$ can be viewed as the energy in $x(t)$ at time t and frequency f. Let $P(t, f) = |X(t, f)|^2$ ($P(t, f)$ is known as the spectrogram of signal $x(t)$). With the STFT-generating TFR, a regional peak search algorithm presented in [32], [39] is introduced. The pseudo code of the algorithm (named 'Algorithm I') is listed in FIGURE 10.

The algorithm presented above searches ridge paths in sub-regions, which increases the accuracy of the extracted ridge path in a noisy environment. The sub-regions are determined by the parameter Δf: a large Δf signifying a wide sub-region and a small Δf indicating a narrow sub-region. Both too large and too small Δf would decrease the accuracy of the algorithm. For rotating machinery, the rotating speed generally does not exhibit a dramatic change; hence, Δf is set as around 2∼5 Hz (2 ∼ 4 times the frequency resolution of STFT-generating TFR). The Δf is set to 5 Hz for simulated and experimental signals in this paper. The key step of the success of 'Algorithm I' is to find a proper starting point for searching as an inappropriate starting point would lead to incorrect ridge path identification. The extensively used method of determining the starting point is to find out the location of the maximum energy in TFR. However, the point with maximum energy does not always correspond to a point right on the IF ridge path of interested signals, particularly for a multi-component signal. It is quite common that when the ridge path of the first signal component is extracted with the starting point corresponding to the one of the maximum energy, ridges paths of remaining signal components cannot be accurately searched started with the point with the maximum energy of the updated TFR as the remaining signal components are often even weaker in terms of energy.

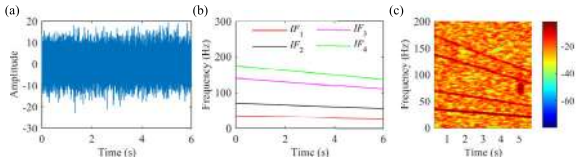

FIGURE 11. (a) The simulated signal, (b) True IF paths of the four signal components, and (c) TFR of (a).

To illustrate, a simulated signal $s(t)$ composing of multiple signal components is taken into consideration:

$$s(t) = \sum_{k=1}^{K} A_k \cos(2\pi \cdot IF_k(t) \cdot t) + n(t), \tag{22}$$

where A_k represents the amplitude of each signal component, $IF_k(t)$ is the IF of each component, $n(t)$ stands for noise as defined in Section 0 and K denote the number of signal components. Four signal components are considered in this example. $IF_1(t)$ is set to be $-2.5t + 35$ and $IF_2(t)$, $IF_3(t)$ and $IF_4(t)$ are equal to $2IF_1(t)$, $4IF_1(t)$, and $5IF_1(t)$, respectively. The amplitude of each component is randomly set 1.5, 0.9, 1.05, and 0.8, respectively. The simulated signal and the IF of each component are shown in FIGURE 11 (a) and (b), respectively. FIGURE 11 (c) presents the TFR of the simulated signal defined by Eq.(22).

The starting point corresponds to the one with maximum energy in the TFR shown in FIGURE 12 (a). With such a starting point, the IF of the first signal component, in FIGURE 12 (b), is successfully extracted using 'Algorithm I'. However, the IFs of the remaining signal component cannot be accurately extracted by 'Algorithm I'. The underlying reason is that points with maximum energy of the updated TFR are not located on IF ridge paths of the signal components. As displayed in FIGURE 12 (c), the second IF is not correctly identified as the starting point with the maximum energy is triggered by interfering signals, rather than signal components. Similarly, the IFs of the third and fourth signal components are not accurately identified as well for the same reason, as shown in FIGURE 12 (e) and (f). Note that the energy distribution of the fourth signal component is not plotted.

To ensure that the selected starting point for searching is located on the IF ridge paths of interested signal components, an improved version of 'Algorithm I' is proposed. IF paths of signal components of interest extracted by 'Algorithm I' are acted as IF pre-estimators denoted by pre-$IF_k(t)$, $k = 12, \ldots, K$, where K represents the number of signal components of interest. The improved algorithm attempts to employ one of the pre-extracted IFs to guide the starting point selection for the rest of signal components. The selected IF used for guidance, denoted by g-$IF(t)$, is the one firstly pre-extracted from TFR, i.e., pre-IF_1, as signal component of the first extracted IF is generally energy-dominant on TFR and it is most likely to be accurately extracted.

Then, a synchronizing operation between g-$IF(t)$ and pre-$IF_k(t)$ is subsequently developed for an appropriate starting

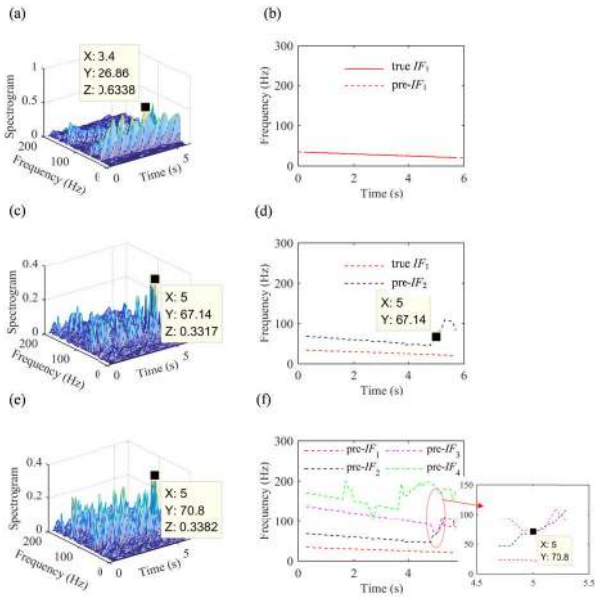

FIGURE 12. Ridge path identification using 'Algorithm I': (a), (c) and (e) Energy distribution of original signal, signal after the first IF path extracted and signal after the first two IF paths extracted, (b) the first identified ridge path and true IF $_1$, (d) the second identified ridge path and true IF $_1$, and (f) four identified IF paths.

point selection for IF extraction. The purpose of the synchronization is to find the synchronization coefficient, named sc_k, which makes the summation of absolute values between g-$IF(t)$ and $IF_{\text{temp}(k)}(t)$ minimal. The $IF_{\text{temp(k)}}(t)$ is defined as

$$IF_{\text{temp}(k)}(t) = \frac{\text{pre-}IF_k(t)}{sc_k}, \tag{23}$$

and the synchronization coefficient sc_k can be obtained by

$$\begin{aligned} sc_k &= \arg\min_{sc} \sum_{m=1}^{M} \left| \text{g-}IF(t_m) - \frac{\text{pre-}IF_k(t_m)}{sc} \right|, \\ sc &= \lambda, 2\lambda, 3\lambda, \ldots, sc_{\max}. \end{aligned} \tag{24}$$

The time instant corresponding to the minimal absolute value between the g-$IF(t)$ and $IF_{\text{temp}(k)}(t)$ is set as the starting point t_{st} for IF extraction.

$$t_{st} = \arg\min_{t_m} \left| \text{g-}IF(t_m) - IF_{\text{temp}(k)}(t_m) \right|, \quad m = 1, 2, \ldots, M, \tag{25}$$

where the parameter λ is the resolution of synchronizing and $sc_{\max}$ is the maximum of synchronization coefficients. The parameter $sc_{\max}$ is specified according to the number of harmonics taken into consideration and the synchronizing resolution λ should be set small enough to make sure that shaft rotating IF, IFCF and their harmonics are not left out. Update the starting point and re-call 'Algorithm I'. The IF of the kth signal component, $IF_k(t)$, can then be accurately extracted. The pseudo code of the improved version of 'Algorithm I' is given in FIGURE 13. In this work, $sc_{\max}$ and λ are respectively set to 20 and 0.01 for simulated and experimental signal analyses. The $sc_{\max}$ equaling 20 is sufficient to cover IFCF, ISRF and a few of their harmonics and λ equaling

The pseudo-code for improved version of 'Algorithm I'
Initialization:
Set parameters, i.e., the number of signal components of interest K, synchronization resolution λ, maximum of synchronization coefficient sc_{max};
Extract pre-estimators of IF, i.e., pre-$IF_k(t)$, using 'Algorithm I' and set the IF for guidance g-$IF(t)$;
While $k \leq K$
  Synchronize g-$IF(t)$ and pre-$IF_k(t)$ by Eqs. (23) and (24) to get the starting point t_{st};
  Re-call 'Algorithm I' to extract $IF_k(t)$;
  Update $k \leftarrow k+1$;
End
Output $IF_1(t), \ldots, IF_k(t), \ldots, IF_K(t)$.

FIGURE 13. Pseudo code of improved version of 'Algorithm I'.

0.01 is small enough to distinguish IFCF, ISRF and their harmonics by ratios among them.

The proposed algorithm is then applied to process the simulated signal defined by Eq.(22). The pre-estimators of IF, i.e., pre-$IF_k(t)$, are extracted by 'Algorithm I' and displayed in FIGURE 12 (f). The first pre-extracted IF is selected as the guidance IF g-$IF(t)$ to update the starting point for the signal components. With the improved algorithm, new starting points for the rest of signal components are searched by finding the minimal absolute value between g-$IF(t)$ and$IF_{\text{temp(k)}}(t)$, as presented in FIGURE 14 (a-c). The synchronizing coefficient sc_k $(k = 1, 2, 3, 4)$ for each signal component is determined as 1, 2, 4 and 5 by the synchronization, respectively, which is identical to the pre-set values. The new starting points, exhibited in FIGURE 14 (a-c), for the second, third and fourth signal components are located at 10, 1 and 12, respectively, indicating that the IFs for the three signal components are obtained by seeking the maximum energy in sub-regions starting at the new points and then moving forwards and backwards till all time instants are taken into consideration. It is worth mentioning that the synchronizing for IF of the first signal component is not plotted in FIGURE 14 since it has been correctly extracted using 'Algorithm I'. The improved version of the algorithm can ensure that starting points of searching are located on the IF paths of signal components; therefore the IFs can be accurately extracted, as shown in FIGURE 14 (d).

C. BEARING FAULT DIAGNOSIS USING THE PROPOSED DUAL-GUIDANCE BASED ORF SELECTION AND MULTIPLE RIDGE PATH IDENTIFICATION

With the determined ORF band and improved algorithm I, the fault-induced impulsive signal can be extracted and the IFCF and its harmonics can be detected. However, the bearing fault type cannot be revealed yet without knowing the FCC. The FCC for bearing with outer race fault (FCC_{o}) and inner race fault (FCC_{I}) under time-varying speed operation can be calculated using

$$IFCF_o = \frac{N_b}{2}\left(1 - \frac{d}{D}\cos\varphi\right) f_r^1 = FCC_{\text{o}} \cdot f_r, \tag{26}$$

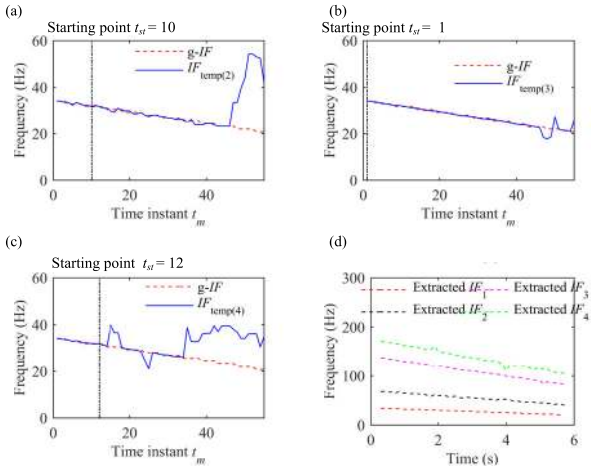

FIGURE 14. Ridge path identification using the improved version of 'Algorithm I': (a-c) the g-IF_1 and the IF_{temp} of the second, third and fourth signal component, respectively, and (d) the identified IF ridge paths of the signal defined by Eq. (22).

$$IFCF_I = \frac{N_b}{2}(1 + \frac{d}{D}\cos\varphi)f_r^1 = FCC_{\mathrm{I}} \cdot f_r, \qquad (27)$$

where N_b represents the number of rolling elements, d is the diameter of the rolling element, D denotes the pitch diameter of the bearing, φ represents the angle of the load from the radial plane, f_r represents the ISRF, and $IFCF_{\mathrm{o}}$ and $IFCF_{\mathrm{I}}$ stand for the IFCF of bearing with outer race fault and inner race fault, respectively. From Eqs. (26) and (27), it can be seen that FCC_{o} and FCC_{I} are only determined by parameters of bearings and independent of shaft rotational speed; hence, they can be employed to perform bearing fault diagnosis under time-varying speed.

In order to calculate FCC, ISRF (denoted by $f_{\mathrm{r}}(t)$) has to be estimated in advance. The ISRF and its harmonics may present in the TFR of envelope of the filtered signal due to amplitude modulation, particularly for inner race fault. They are also very likely to present in low frequency band because of misalignment, imbalanced mass or eccentricity caused by manufacturing or/and mounting errors etc. [31], [40]. Therefore, to make sure the ISRF and its harmonics can be extracted, the frequency band of collected vibration is chopped and the signal of low frequency band is obtained using a low-pass filter. The cut-off frequency of the low-pass filter is user-specified and set to cover the ISRF and a few of its harmonics. The ridge paths of the ISRF and its harmonics can be identified using the proposed algorithm in section 0. It has to be noted that it cannot be guaranteed that the first extracted ridge path just happens to be the ISRF; however, the ISRF can be always extracted using the proposed algorithm because the sub-regions are set to zero after the extraction of the previous ridge paths. The bearing fault diagnosis can then be implemented via matching the average ratios of the extracted $IFCF_i(t)$ $(i = 1, 2, 3, \ldots)$ to $f_r^j(t)$ $(j = 1, 2, 3, \ldots)$ to FCC and its multiples, where $IFCF_i(t)$ represents the ith extracted IFCF-related IF path and $f_r^j(t)$ stands for the jth extracted ISRF-related IF path.

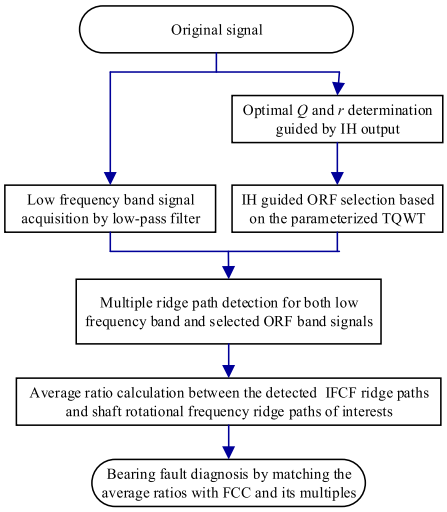

FIGURE 15. Flowchart of the bearing fault diagnosis.

The average ratio between $IFCF_i(t)$ and the first extracted ISRF-related IF$f_r^1(t)$ can be expressed as

$$R_i^1 = \frac{1}{M}\sum_{m=1}^{M}\frac{IFCF_i(t_m)}{f_r^1(t_m)}, \quad i = 1, 2, \ldots, imax, \qquad (28)$$

where M is the number of time instant as defined previously, $imax$ denotes the number of extracted IFCF-related ridge paths. The average ratio R_i^j of $IFCF_i(t)$ to $f_r^j(t)$, $(j = 2, 3, \ldots)$ can be calculated in the same manner. Let a vector $\boldsymbol{R^j} = [R_1^j, R_2^j, \ldots, R_i^j, \ldots, R_{imax}^j]$, i.e., the vector $\boldsymbol{R^j}$, named diagnosis vector, represents the average ratios of $imax$ IFCF-related ridge paths to the jth ISRF-related IF path. Based on the statement presented above, the bearing fault diagnosis procedure can be summarized using a flowchart of FIGURE 15.

IV. VALIDATIONS

To exam the performance of the proposed method, experimental signals contaminated by interferences transmitted from a gearbox and noise are collected on a SpectraQuest machinery fault simulator (MFS-PK5MT). Vibration signals from both outer race fault and inner race fault are measured.

A. BEARING OUTER RACE FAULT DIAGNOSIS

The experimental setup for outer race fault is shown in FIGURE 16, where two ER16K bearings are utilized to support the shaft of 1 inch in diameter and a mass of 5.03 kg is mounted on the shaft as an external load. The bearing shaft is driven by an AC converter controlled motor through a coupling. The right side is connected to the gearbox shaft by belts and two sheaves (the smaller one is fixed on the bearing shaft and the larger one is installed on the gearbox shaft). Detailed parameters of the bearing are listed in TABLE 3. The motor shaft rotational speed rises from 35.3 Hz to 60.7 Hz following a nonlinear manner. The sampling frequency is 20 kHz. In addition, as shown in FIGURE 16, a tachometer

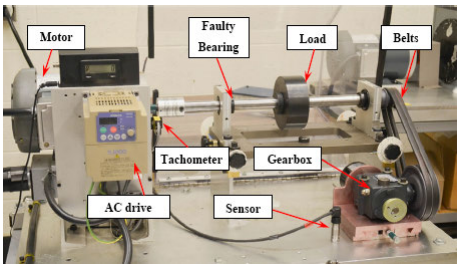

FIGURE 16. Experimental setup for outer race fault.

TABLE 3. Parameters of the bearings used in the test.

Bearing type	Pitch diameter (mm)	Ball diameter (mm)	Number of balls	IFCF of outer race fault (Hz)	IFCF of inner race fault (Hz)	Number of gear teeth	Diameter ratio of sheaves
ER16 K	38.52	7.94	9	$5.43f_r$	$3.57f_r$	18	1:2.6

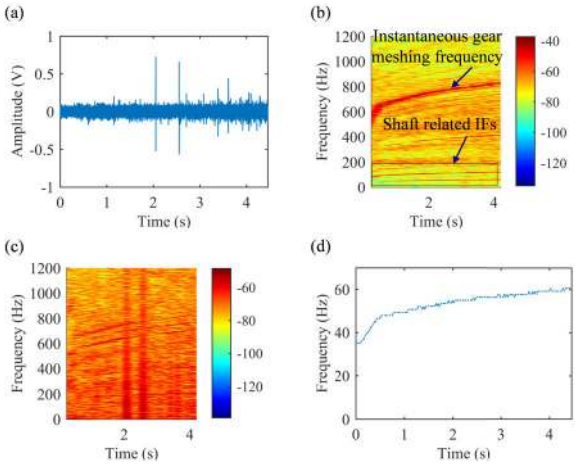

FIGURE 17. Collected vibration signal and TFA for outer race fault case: (a) raw signal, (b) TFR of the raw signal, (c) TFR of the envelope of the raw signal, and (d) Collected ISRF.

is used to collect the instantaneous shaft rotational speed for the purpose of verifying the proposed method.

The collected raw signal is shown in FIGURE 17 (a). FIGURE 17 (b) and (d) exhibit the TFR of the raw signal and its envelope signal, respectively. It can be seen that the instantaneous gear meshing frequency dominates the TFR of the raw vibration signal. In addition, a few of shaft related IF components can also be observed in FIGURE 17 (b). However, IFCF and its harmonics cannot be identified. In terms of the TFR of envelope of the raw signal, no clear TF ridges can be recognized, as presented in FIGURE 17 (c). The collected shaft rotational speed is shown in FIGURE 17 (d), which can be used to verify the estimated IF obtained by the improved algorithm.

The proposed dual-guidance based scheme is then adopted to process the collected signal. To determine the TQWT-related parameters, Q-factor versus IH output scatter diagram is plotted in FIGURE 18 (a), showing that the determined Q and r is 8 and 6, respectively. The corresponding frequency responses are presented in FIGURE 18 (b). According to Eq. (19), there are 91 stages, i.e., 91 sub-signals. The normalized kurtosis, CF and reciprocal of SI values of each sub-signals are calculated, as exhibited in FIGURE 18 (c), from which it can be observed that the peak intervals (indicated by n and n') of the three indicators are situated in different positions. Weight vectors are then calculated via step 2 in sub-section 0. The obtained weight vectors of the three indexes are displayed in FIGURE 18 (d). The IH output of the indexes of each merged signal is calculated during merging, shown in FIGURE 18 (e). The maximum of IH output corresponds to the 3rd merged signal which contains 8 original sub-signals from the 6th to 13th according the merged sub-band filters in FIGURE 18 (f). By observing FIGURE 18 (f), parameters m and k can be determined as 8 and 6, respectively. The selected ORF band, FIGURE 18 (g), is centralized around 6470 Hz with the bandwidth 1699 Hz. The raw signal is subsequently filtered using the determined ORF band. The band-pass filtered signal is shown in FIGURE 18 (h). FIGURE 18 (i) and (j) exhibit the frequency spectrum of the filtered signal and the TFR of its envelope. The spectrum further indicates that the frequency of filtered signal is around 6470 Hz. With the weight vectors, the effects of index values caused by noise and interferences are weakened and contribution of index values arisen by target signal is kept when calculating IH output. Then, the ORF can be successfully selected. From the TFR of envelope of the filtered signal, two IF paths which are likely to be IFCF-related ridge paths can be easily recognized. However, the final diagnosis result cannot be made yet without knowing the ISRF information because there is a possibility that the two IF paths may relate to ISRF or other components, rather than IFCF and its harmonics, even though this rarely happens. Furthermore, even if the two IF paths are related to IFCF, the fault type cannot be determined yet without ISRF information.

To complete the diagnosis, ISRF related ridge paths are also required to be extracted and average ratios among the extracted ridge paths have to be calculated, in addition to IFCF related ridge paths. The diagnosis results can then be made by matching the average ratios to bearing FCCs and its multiples. The 'Algorithm I' is applied to extracting the pre-estimator of IFCF-related paths, i.e., pre-*IFCF*, and the extracted results are presented in FIGURE 19 (b). As seen, the IFCF_1 can be accurately extracted using 'Algorithm I'. This is because the maximal energy is located on IFCF-related path, as shown in FIGURE 19 (a).

Then, the improved version of 'Algorithm I' is used. The extracted IFCF_1 acts as the guidance IF. The synchronization is performed and the synchronization coefficient sc_2 is found to be 2. As shown in FIGURE 19 (c), the starting point of searching is located at the 38th time instance, where absolute value between $IFCF_1(t)$ and $IF_{temp(2)}(t)$ is minimal, instead of the one with maximum energy which might be caused by interfering signals. With the new starting point, the $IFCF_2$ is extracted, as displayed in FIGURE 19 (d) (black solid line).

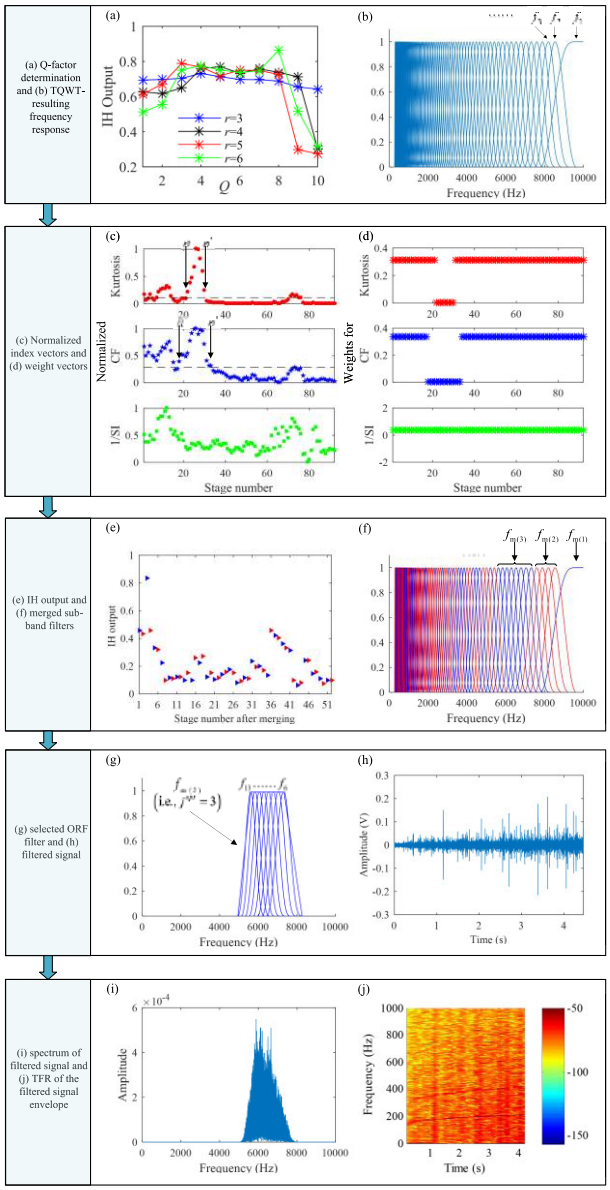

FIGURE 18. ORF selection using the proposed dual-guidance based scheme for bearing outer race fault diagnosis.

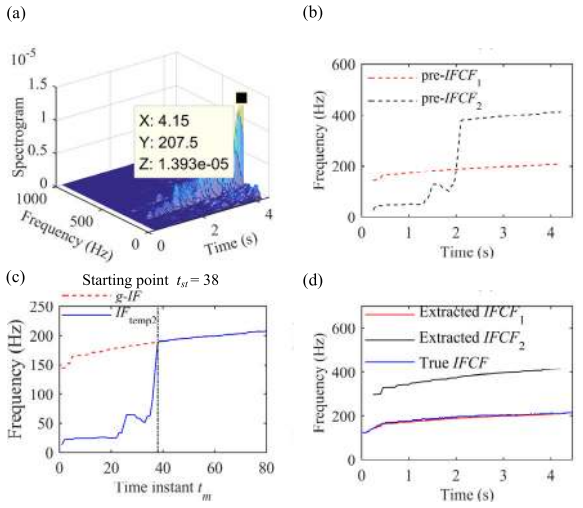

FIGURE 19. Multiple ridge path identification using the improved version of 'Algorithm I' for band-pass filtered signal from the bearing with an outer race fault: (a) energy distribution of the filtered signal, (b) pre- *IFCF* obtained by 'Algorithm I', (c) synchronized $IFCF_2$ and extracted $IFCF_1$, and (d) extracted IFCF-related paths and true IFCF.

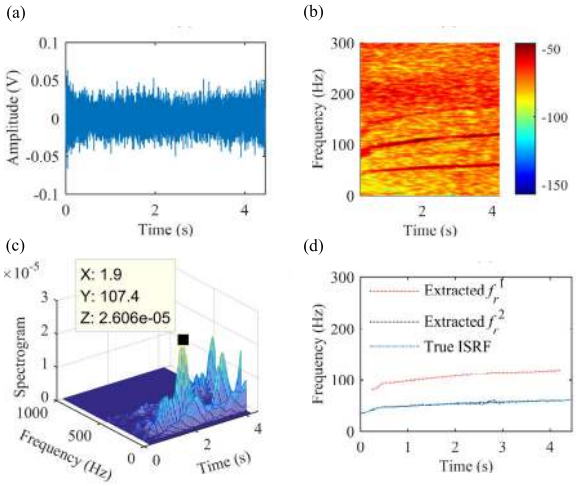

FIGURE 20. Multiple ridge path identification for lower frequency band signal from the bearing with an outer race fault: (a) low-pass filtered signal; (b) TFR of the filtered signal; (c) energy distribution of the filtered signal, and (d) extracted ISRF-related ridges using 'Algorithm I'.

The lower frequency band signal is obtained by a low-pass filter with the cut-off frequency 500 Hz. The filtered signal and its envelope spectra are shown in FIGURE 20 (a) and (b), respectively. Two IF ridges can be clearly discerned in FIGURE 20 (b). By 'Algorithm I', the results are shown in FIGURE 20 (d), showing that the first ISRF-related path is accurately extracted. This is also echo with FIGURE 20 (c), where the maximal energy is situated in the ISRF-related path. In this case, the second ISRF-related IF is also successfully detected by 'Algorithm I', as shown in FIGURE 20 (d). It is worth mentioning that the second harmonic of ISRF is extracted prior to ISRF in this circumstance.

Given the extracted IFCF-related ridges and IRSF-related ridges, the average ratios among them can be calculated using Eq. (28), as presented in FIGURE 21. The vector $\mathbf{R}^1$ represents the average ratios of the extracted IFCF-related ridges $IFCF_i(t)$ $(i = 1, 2)$ to first extracted ISRF ridge $f_r^1(t)$, i.e., $\frac{1}{M}\sum_{m=1}^{M}\frac{IFCF_1(t_m)}{f_r^1(t_m)}$ and $\frac{1}{M}\sum_{m=1}^{M}\frac{IFCF_2(t_m)}{f_r^1(t_m)}$ for the outer race case. Likewise, the vector $\mathbf{R}^2$ represents average ratios of the extracted $IFCF_i(t)$ $(i = 1, 2)$ to the second extracted ISRF-related ridge $f_r^2(t)$, i.e., $\frac{1}{M}\sum_{m=1}^{M}\frac{IFCF_1(t_m)}{f_r^2(t_m)}$ and $\frac{1}{M}\sum_{m=1}^{M}\frac{IFCF_2(t_m)}{f_r^2(t_m)}$. By observing the average ratios in FIGURE 21, it can be found that 3.49 matches to FCC_o (3.57), 6.98 equals to $2\times FCC_o$ and 1.74 is around half of FCC_o. It can be concluded that the first extracted ISRF-related path is the second harmonic of ISRF and the second extracted path is the ISRF. It can also be confirmed that the bearing has a local fault on the outer race.

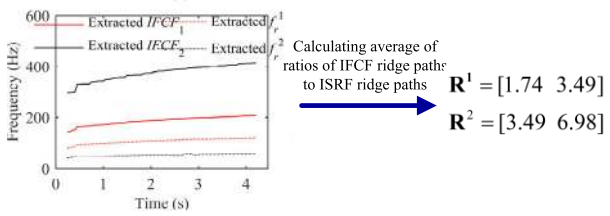

FIGURE 21. Multiple ridge paths from lower frequency band signal and ORF band signal.

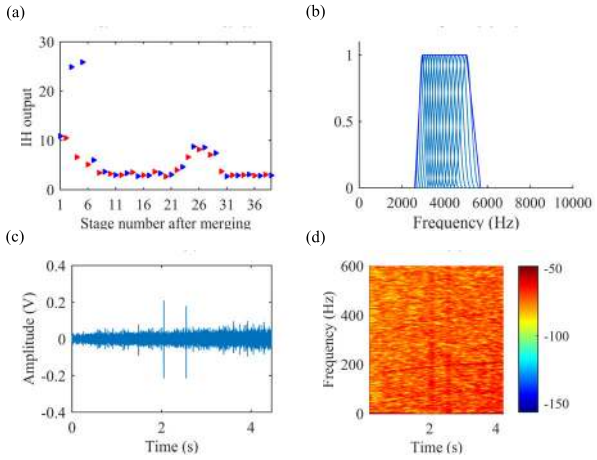

FIGURE 22. ORF band selection using the original criterion fusion strategy for bearing outer race fault diagnosis: (a) IH output of each merged signal; (b) selected ORF band; (c) filtered signal using the selected ORF band; and (d) TFR of the filtered signal.

For comparison, the original criterion fusion strategy is applied for ORF band determination of the signal from the bearing with an outer race fault. Merging results in FIGURE 22 (a) shows that there are 39 signal components after merging and the 5th merged signal containing 15 sub-signals generates the maximum IH output. Accordingly, the selected ORF band is centered at 4140 Hz with the bandwidth 3074 Hz, as shown in FIGURE 22 (b). The raw signal is then filtered using the selected ORF band, followed by TFA of the envelope of the filtered signal in FIGURE 22 (c). The resulting TFR is presented FIGURE 22 (d), where IF ridges can barely be recognized. The weights for kurtosis, CF and SI index are 0.3149, 0.3361 and 0.3490, respectively, thus it cannot highlight the index which truly reflects the impulsiveness.

B. BEARING INNER RACE FAULT DIAGNOSIS

To further investigate the performance of the proposed method, it is applied for bearing inner race fault diagnosis in this sub-section. The experiment is shown in FIGURE 23. Two ER16K bearings, the same as the ones in outer race fault diagnosis experimental setup, are used. Unlike the outer race fault case, the accelerometer is positioned right on the top of the faulty bearing. The bearing parameters have been listed in Table 3. A tachometer and accelerometer are mounted on the test rig to collect the shaft speed and vibration signal,

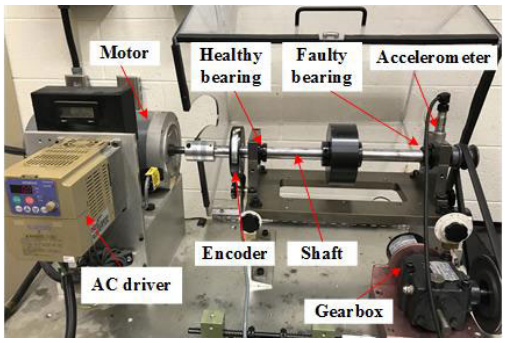

FIGURE 23. Experimental setup for bearing inner race diagnosis.

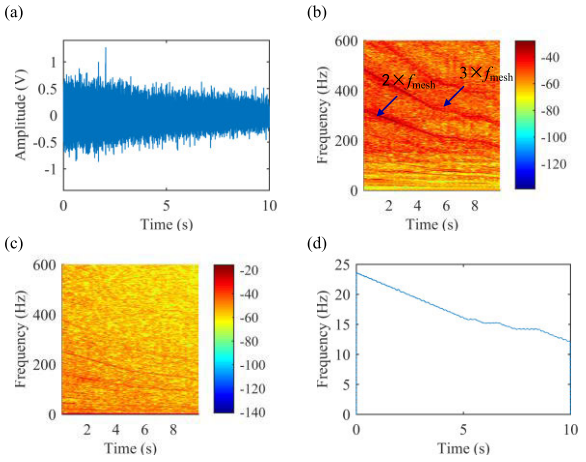

FIGURE 24. Collected vibration signal and TFA for inner race fault case: (a) the raw signal, (b) TFR of the raw signal, (c) TFR of the envelope of the raw signal, and (d) Collected ISRF.

respectively. Similar to the outer race fault case, the shaft speed is measured for the purpose of validation. The signal is sampled at a rate of 20 kHz for 10 s. The ISRF decreases from 24 Hz to 12 Hz.

The collected raw signal and shaft rotational speed are shown in FIGURE 24 (a) and (d), respectively. As stated above, the ISRF plotted in FIGURE 24 (d) declines from 24 Hz to 12 Hz during 10 s. The TFR of the raw signal is presented in FIGURE 24 (b). As shown, the TFR of the raw signal is dominated by harmonics of gear meshing frequency f_{mesh} and thus no information related to bearing fault can be revealed. FIGURE 24 (c) shows the blurry TFR of the envelope of the raw signal, from which no clear IF ridges can be seen due to the existence of interfering signals.

Applying the proposed method for the raw signal, the optimal parameters Q and r are selected as 7 and 4, respectively, according to FIGURE 25 (a). The frequency responses with 53 stages resulted by parametrized-TQWT are given in FIGURE 25 (b). For each stage, kurtosis, CF and reciprocal of SI are calculated. The normalized vectors are shown in FIGURE 25 (c). The locations of peak interval, indicated in FIGURE 25 (c), of the three indexes are different; therefore, weight vectors are calculated, as presented in FIGURE 25 (d). Then the IH output is calculated using Eq. (13) for merging

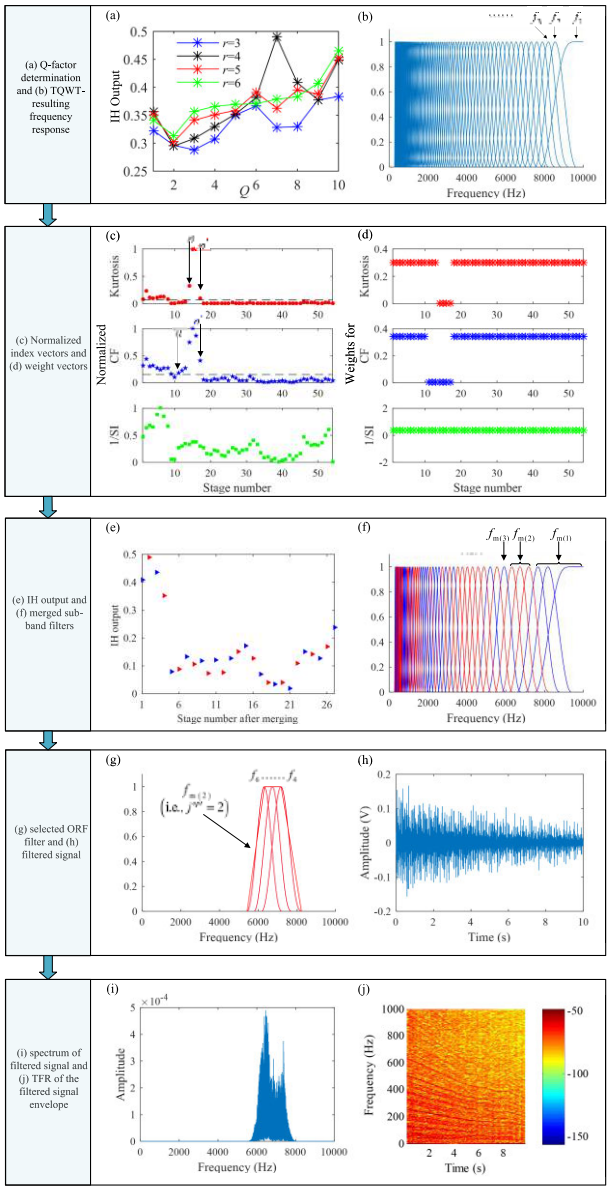

FIGURE 25. ORF selection using the proposed dual-guidance based method for bearing inner race fault diagnosis.

operation. After merging, the IH output of each merged signal is displayed in FIGURE 25 (e), from which it can be observed that the second merged signal containing 3 sub-signals (from the 4th to 6th) has the maximum IH output. The merged sub-band filters are exhibited in FIGURE 25 (f), from which it can be seen that m and k equal to 3 and 4, respectively, indicating that there are three sub-band filters composed the select ORF starting from the 4th sub-band filter. The selected ORF is presented in FIGURE 25 (g) with frequency center 6760 Hz and bandwidth 871 Hz. The raw signal is then filtered by the selected ORF band, with the result presented in FIGURE 25 (h). The spectrum of the filtered signal and TFR of its envelope are plotted in FIGURE 25 (i) and (j), respectively, showing that the filter signal is centered around 6760 Hz and a few of IF ridges can be identified in the TFR of

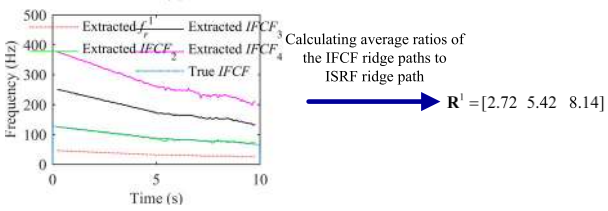

FIGURE 26. Multiple ridge path identification using the improved version of 'Algorithm I' for band-pass filtered signal from the bearing with an inner race fault.

the filtered signal. Compared with the TFR of the raw signal envelope in FIGURE 24 (c), the filtered signal is dominated by impulsive signals and the other interfering signal has been removed. However, it cannot determine what these IF ridges represent and what the fault type is yet.

The improved version of 'Algorithm I' is then applied for IF ridge extractions. FIGURE 26 presents the extraction results. The details about performing the improved algorithm are not given in the paper since they are similar to those of the outer race fault diagnosis. The extracted IFCF-related path and ISRF-related path are shown in FIGURE 26. The true IFCF is also plotted in FIGURE 26 for comparison. To conduct bearing fault diagnosis, the average ratios of the IF ridge positioned in the very bottom of TFR and other three IF ridges are calculated, which forms a vector $\mathbf{R}^1$ shown in FIGURE 26. By observing this vector, the second element 5.42 matches the FCC_I(=5.43) very well. The first element is half of the second one and the third one is 1.5 times of the second one. It then can be concluded that the extracted ISRF-related path is the second harmonic of ISRF and the bearing is inner race defective.

It has to mention that, unlike the outer race fault diagnosis, the lower frequency band signal is not discussed for the inner race fault case and the diagnosis can be completed without being adversely affected. The reason is that the ISRF-related IF ridges can also be extracted from the band-pass filtered signal in the inner case as the amplitude modulation often happens.

Additionally, the original criterion fusion strategy is also used to filter the raw signal for comparison. The IH output is shown in FIGURE 27 (a) and the selected frequency band is shown in FIGURE 27 (b). The center of the selected frequency band is around 4000 Hz with the bandwidth of 1780 Hz. Filtering the raw signal by the selected frequency band, the filtered signal and TFR of its envelope are displayed in FIGURE 27 (c) and (d), respectively. Apparently, the TFR in FIGURE 27 (d) is more obscure than the one in FIGURE 25 (j). The comparison indicates that the proposed IH guided ORF scheme outperforms the original one. The calculated weights of kurtosis, CF and SI vector of the original hybrid method are 0.3023, 0.3400 and 0.3577. Similar to outer race case, no obvious difference among the weights; hence index values triggered by impulsive noise cannot be distinguished from the ones caused by target impulsive signals, resulting in failure of ORF selection.

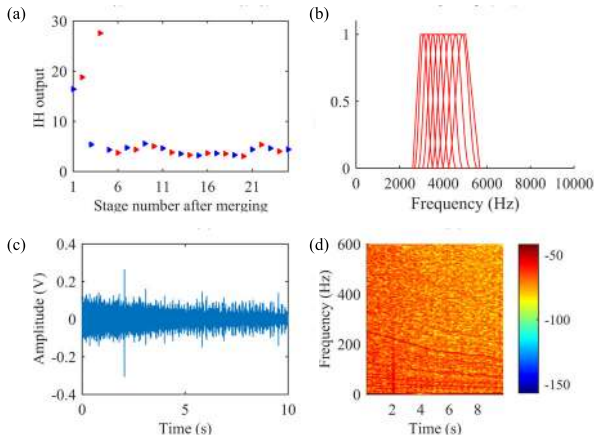

FIGURE 27. ORF band selection using the original criterion fusion strategy for bearing inner race fault diagnosis: (a) IH output of each merged signal; (b) selected ORF band; (c) filtered signal using the selected ORF band; and (d) TFR of the filtered signal.

TABLE 4. Executing time of the proposed method for experimental data analysis (related to ORF band determination and multiple IF path identification).

	Sampling frequency (kHz)	Signal length (s)	Number of sub-signals / identified IF paths	Processing time (s)		Average processing time for 1s data (s)	
				ORF selection	Multiple IF path extraction	ORF selection	Multiple IF path extraction
outer race fault	20	4.457	91/4	35.694	0.252	8	0.057
Inner race fault	20	10	53/4	23.4	0.348	2.34	0.0348

The computational cost the algorithm is important for industrial applications, particularly for on-line fault diagnosis. To give information about the computational efficiency of the proposed ORF selection method and multiple IF path identification method, the executing times for experimental data processing are listed in Table 4. The algorithms are executed by MATLAB 2014b on the Laptop running Windows 10 with an Intel Core i7-8550U 1.8GHz processor and 8.00 GB of RAM. It can be seen from Table 4 that: 1) the computational cost of ORF selection is dependent on the signal length, the number of sub-signals and signal types, and the computational efficiency of multiple IF extraction algorithm relies upon the signal length, the number of extracted IF paths and signal types; and 2) the peak search based multiple IF extraction algorithm is quite computationally effective, much more efficiency than the ORF selection algorithm.

For optimal Q and r combination selection, the computational time is more expensive as all possible combinations have to be considered to find the optimal one. The computational time of identifying optimal Q and r combination for outer race and inner race fault signal is respectively around 8 min and 11.5 min using the same Laptop. However, it is worth mentioning that the procedure of determining optimal Q and r is not mandatory for the success of the proposed method for bearing fault diagnosis. The resonant frequency band can still be detected without the strategy of determining optimal Q and r combination; but it may be not the optimal one. For real applications, if the first priority is given on the time effectiveness it is not recommended to involve the procedure of finding optimal Q and r. Otherwise, the strategy for optimal parameter combination can be executed to obtain the optimal frequency band for filtering. Additionally, it is noteworthy that, if the procedure of optimal Q and r combination is not involved, larger Q and r values are recommended. Then, frequency resolution of frequency response would be higher and an inefficient filter, such as the 1st frequency response in Fig.3, can be avoided.

V. CONCLUSION AND DISCUSSIONS

A. CONCLUSIONS

This paper proposes a technique to address the main challenges of bearing fault diagnosis under time-varying speed conditions. The proposed method contains two parts: the dual-guidance based ORF selection scheme with TQWT embedded and multiple IF ridge identification by the improved peak search algorithm. The former is designed to maximally extract defect-induced fault signature under variable speed conditions and the latter is devoted to identifying multiple IF ridges from TFR of the extracted fault signatures. Given the identified ridges, the fault diagnosis can then be effectively conducted without relying upon tachometers and resampling, which expands the industrial application of the proposed technique.

The developed dual-guidance based scheme with TQWT embedded exploits non-fixed weights for the index vectors, resolving the drawback of the existing criterion fusion method where constant weights are used. Furthermore, the frequency band segmentation is realized via frequency responses of TQWT, instead of equal division, which satisfies the frequency resolution requirement that high frequency band accepts a lower frequency resolution and low frequency band needs a higher frequency resolution for signal analysis. The optimal TQWT related parameters are also determined based on IH output. With the extracted impulses, multiple IF ridge identification algorithm is devised for fault diagnostics. The algorithm not only keeps the simple yet computationally effective advantage of the fundamental peak search algorithm, but also can accurately identify IF ridges with the synchronization step.

In addition, the motivation of the proposed dual-guidance based ORF selection scheme is illustrated and the comparison between the original peak search algorithm and improved one is also performed. Experimental investigations are executed to have tested the effectiveness of the proposed techniques.

B. DISCUSSIONS

Segmenting frequency bands using TQWT has limitations. The frequency range that TQWT frequency response can cover is dependent on signal length, in addition to Q-factor and redundancy. If the target frequency is quite low and, unfortunately, meanwhile the signal length is quite short, the target frequency may not be able to be detected. Besides, finding optimal Q and r combination is time consuming;

thus, the future work can be conducted on the direction of determining optimal Q and r efficiently.

Lastly, it is worth mentioning that the function used for weight vector calculation is not smooth, where, as long as needed, the weights for index points are set zero. In future work, this function still has the room for improvements. In addition, identifying two or even multiple ORF band is also recommended for future work.

ACKNOWLEDGMENT

The authors would like to thank the Lab E026 in the University of Ottawa for the data collection.

REFERENCES

[1] L. Cui, X. Gong, J. Zhang, and H. Wang, "Double-dictionary matching pursuit for fault extent evaluation of rolling bearing based on the Lempel-Ziv complexity," *J. Sound Vib.*, vol. 385, pp. 372–388, Dec. 2016.
[2] H. Wang, P. Wang, L. Song, B. Ren, and L. Cui, "A novel feature enhancement method based on improved constraint model of online dictionary learning," *IEEE Access*, vol. 7, pp. 17599–17607, 2019.
[3] D. Wang, P. W. Tse, and Y. L. Tse, "A morphogram with the optimal selection of parameters used in morphological analysis for enhancing the ability in bearing fault diagnosis," *Meas. Sci. Technol.*, vol. 23, no. 6, pp. 65001–65015, 2012.
[4] J. Shi and M. Liang, "Intelligent bearing fault signature extraction via iterative oscillatory behavior based signal decomposition (IOBSD)," *Expert Syst. With Appl.*, vol. 45, pp. 40–55, Mar. 2016.
[5] L. Wang and J. Xiang, "A two-stage method using Spline-Kernelled chirplet transform and angle synchronous averaging to detect faults at variable speed," *IEEE Access*, vol. 7, pp. 22471–22485, 2019.
[6] J. Urbanek, T. Barszcz, N. Sawalhi, and R. Randall, "Comparison of amplitude-based and phase-based methods for speed tracking in application to wind turbines," *Metrol. Meas. Syst.*, vol. 18, no. 2, pp. 295–304, 2011.
[7] P. Borghesani, R. Ricci, S. Chatterton, and P. Pennacchi, "Diagnostic of rolling element bearings with envelope analysis in non-stationary conditions," in *Advances in Condition Monitoring of Machinery in Non-Stationary Operations*. Berlin, Germany: Springer, 2014, pp. 127–135.
[8] K. R. Fyfe and E. D. S. Munck, "Analysis of computed order tracking," *Mech. Syst. Signal Process.*, vol. 11, no. 2, pp. 187–205, 1997.
[9] A. B. Ming, W. Zhang, Z. Y. Qin, and F. L. Chu, "Fault feature extraction and enhancement of rolling element bearing in varying speed condition," *Mech. Syst. Signal Process.*, vols 76–77, pp. 367–379, Aug. 2016.
[10] P. D. McFadden and J. D. Smith, "Vibration monitoring of rolling element bearings by the high-frequency resonance technique—A review," *Tribol. Int.*, vol. 17, no. 1, pp. 3–10, 1984.
[11] W. Guo, X. Jiang, N. Li, J. Shi, and Z. Zhu, "A coarse TF ridge-guided multi-band feature extraction method for bearing fault diagnosis under varying speed conditions," *IEEE Access*, vol. 7, pp. 18293–18310, 2019.
[12] J. Lin and L. Qu, "Feature extraction based on Morlet wavelet and its application for mechanical fault diagnosis," *J. Sound Vib.*, vol. 234, no. 1, pp. 135–148, Jun. 2000.
[13] H. Qiu, J. Lee, J. Lin, and G. Yu, "Wavelet filter-based weak signature detection method and its application on rolling element bearing prognostics," *J. Sound Vib.*, vol. 289, nos. 4–5, pp. 1066–1090, 2006.
[14] I. S. Bozchalooi and M. Liang, "A joint resonance frequency estimation and in-band noise reduction method for enhancing the detectability of bearing fault signals," *Mech. Syst. Signal Process.*, vol. 22, no. 4, pp. 915–933, 2008.
[15] I. S. Bozchalooi and M. Liang, "A smoothness index-guided approach to wavelet parameter selection in signal de-noising and fault detection," *J. Sound Vib.*, vol. 308, nos. 1–2, pp. 246–267, 2007.
[16] W. He, Z.-N. Jiang, and K. Feng, "Bearing fault detection based on optimal wavelet filter and sparse code shrinkage," *Measurement*, vol. 42, no. 7, pp. 1092–1102, 2009.
[17] D. Wang, S. Sun, and P. W. Tse, "A general sequential Monte Carlo method based optimal wavelet filter: A Bayesian approach for extracting bearing fault features," *Mech. Syst. Signal Process.*, vols. 52–53, pp. 293–308, Feb. 2015.
[18] J. Antoni and R. B. Randall, "The spectral kurtosis: Application to the vibratory surveillance and diagnostics of rotating machines," *Mech. Syst. Signal Process.*, vol. 20, no. 2, pp. 308–331, 2006.
[19] J. Antoni, "Fast computation of the kurtogram for the detection of transient faults," *Mech. Syst. Signal Process.*, vol. 21, no. 1, pp. 108–124, 2007.
[20] Y. Lei, J. Lin, Z. He, and Y. Zi, "Application of an improved kurtogram method for fault diagnosis of rolling element bearings," *Mech. Syst. Signal Process.*, vol. 25, no. 5, pp. 1738–1749, 2011.
[21] D. Wang, P. W. Tse, and K. L. Tsui, "An enhanced Kurtogram method for fault diagnosis of rolling element bearings," *Mech. Syst. Signal Process.*, vol. 35, nos. 1–2, pp. 176–199, Feb. 2013.
[22] T. Barszcz and A. JabŁoński, "A novel method for the optimal band selection for vibration signal demodulation and comparison with the Kurtogram," *Mech. Syst. Signal Process.*, vol. 25, no. 1, pp. 431–451, 2011.
[23] B. Chen, Z. Zhang, Y. Zi, Z. He, and C. Sun, "Detecting of transient vibration signatures using an improved fast spatial-spectral ensemble kurtosis kurtogram and its applications to mechanical signature analysis of short duration data from rotating machinery," *Mech. Syst. Signal Process.*, vol. 40, no. 1, pp. 1–37, 2013.
[24] A. Moshrefzadeh and A. Fasana, "The Autogram: An effective approach for selecting the optimal demodulation band in rolling element bearings diagnosis," *Mech. Syst. Signal Process.*, vol. 105, pp. 294–318, May 2018.
[25] J. Antoni, "The infogram: Entropic evidence of the signature of repetitive transients," *Mech. Syst. Signal Process.*, vol. 74, pp. 73–94, Jun. 2016.
[26] X. Xu, Z. Qiao, and Y. Lei, "Repetitive transient extraction for machinery fault diagnosis using multiscale fractional order entropy infogram," *Mech. Syst. Signal Process.*, vol. 103, pp. 312–326, Mar. 2018.
[27] N. G. Nikolaou and I. A. Antoniadis, "Demodulation of vibration signals generated by defects in rolling element bearings using complex shifted Morlet wavelets," *Mech. Syst. Signal Process.*, vol. 16, no. 4, pp. 677–694, 2002.
[28] C. Li, M. Liang, and T. Wang, "Criterion fusion for spectral segmentation and its application to optimal demodulation of bearing vibration signals," *Mech. Syst. Signal Process.*, vols. 64–653, pp. 132–148, Dec. 2015.
[29] S. Lu, R. Yan, Y. Liu, Q. Wang, "Tacholess speed estimation in order tracking: A review with application to rotating machine fault diagnosis," *IEEE Trans. Instrum. Meas.*, vol. 68, no. 7, pp. 2315–2332, Jul. 2019.
[30] J. Shi, M. Liang, D.-S. Necsulescu, and Y. Guan, "Generalized stepwise demodulation transform and synchrosqueezing for time-frequency analysis and bearing fault diagnosis," *J. Sound Vib.*, vol. 368, pp. 202–222, Apr. 2016.
[31] H. Huang, N. Baddour, and M. Liang, "Bearing fault diagnosis under unknown time-varying rotational speed conditions via multiple time-frequency curve extraction," *J. Sound Vib.*, vol. 414, pp. 43–60, Feb. 2018.
[32] B. Barkat and K. Abed-Meraim, "Algorithms for blind components separation and extraction from the time-frequency distribution of their mixture," *EURASIP J. Adv. Signal Process.*, vol. 2004, no. 13, pp. 2025–2033, 2004.
[33] T. Wang, M. Liang, J. Li, and W. Cheng, "Rolling element bearing fault diagnosis via fault characteristic order (FCO) analysis," *Mech. Syst. Signal Process.*, vol. 45, no. 1, pp. 139–153, 2014.
[34] I. W. Selesnick, "Wavelet transform with tunable Q-factor," *IEEE Trans. Signal Process.*, vol. 59, no. 8, pp. 3560–3575, Aug. 2011.
[35] J. Luo, D. Yu, and M. Liang, "A kurtosis-guided adaptive demodulation technique for bearing fault detection based on tunable-Q wavelet transform," *Meas. Sci. Technol.*, vol. 24, no. 5, 2013, Art. no. 055009.
[36] J. Shi, M. Liang, and Y. Guan, "Bearing fault diagnosis under variable rotational speed via the joint application of windowed fractal dimension transform and generalized demodulation: A method free from prefiltering and resampling," *Mech. Syst. Signal Process.*, vols. 68–69, pp. 15–33, Feb. 2016.
[37] I. Djurović and L. Stanković, "An algorithm for the Wigner distribution based instantaneous frequency estimation in a high noise environment," *Signal Process.*, vol. 84, no. 3, pp. 631–643, 2004.
[38] D. Iatsenko, P. V. E. McClintock, and A. Stefanovska, "Extraction of instantaneous frequencies from ridges in time-frequency representations of signals," *Signal Process.*, vol. 125, no. 1, pp. 290–303, Aug. 2016.
[39] N. A. Khan and B. Boashash, "Instantaneous frequency estimation of multicomponent nonstationary signals using Multiview time-frequency distributions based on the adaptive fractional spectrogram," *IEEE Signal Process. Lett.*, vol. 20, no. 2, pp. 157–160, Feb. 2013.
[40] Y. Wang, G. Xu, A. Luo, L. Liang, and K. Jiang, "An online tacholess order tracking technique based on generalized demodulation for rolling bearing fault detection," *J. Sound Vib.*, vol. 367, pp. 233–249, Apr. 2016.